

# Averaging over atom snapshots in linear-response TDDFT of disordered systems: A case study of warm dense hydrogen

Zhandos A. Moldabekov,<sup>1,2,\*</sup> Jan Vorberger,<sup>2</sup> Mani Lokamani,<sup>3</sup> and Tobias Dornheim<sup>1,2</sup>

<sup>1</sup>*Center for Advanced Systems Understanding (CASUS), D-02826 Görlitz, Germany*

<sup>2</sup>*Helmholtz-Zentrum Dresden-Rossendorf (HZDR), D-01328 Dresden, Germany*

<sup>3</sup>*Information Services and Computing, Helmholtz-Zentrum Dresden-Rossendorf (HZDR), D-01328 Dresden, Germany*

Linear-response time-dependent density functional theory (LR-TDDFT) simulations of disordered extended systems require averaging over different snapshots of ion configurations to minimize finite size effects due to the snapshot-dependence of the electronic density response function and related properties. We present a consistent scheme for the computation of the macroscopic Kohn-Sham (KS) density response function connecting an average over snapshot values of charge density perturbations to the averaged values of KS potential variations. This allows us to formulate the LR-TDDFT within the adiabatic (static) approximation for the exchange-correlation (XC) kernel for disordered systems, where the static XC kernel is computed using the direct perturbation method [Moldabekov *et al.* J. Chem. Theory Comput. **19**, 1286 (2023)]. The presented approach allows one to compute the macroscopic dynamic density response function as well as the dielectric function with a static XC kernel generated for any available XC functional. The application of the developed workflow is demonstrated for the example of warm dense hydrogen. The presented approach is applicable for various types of extended disordered systems such as warm dense matter, liquid metals, and dense plasmas.

## I. INTRODUCTION

*Ab initio* simulations play an indispensable role in the understanding of the physics and chemistry of materials at extreme conditions. Such warm dense matter (WDM) naturally appears in the interiors of planets [1], brown dwarfs [2], and white dwarfs [3], and in the outer layer of relatively cold neutron stars [4]. In experiments, WDM is created using powerful lasers and shock compression at facilities such as the National Ignition Facility (NIF) [5–7] and the European X-ray Free-Electron Laser (XFEL) [8, 9]. Without accurate simulations, the extreme conditions and the short life time of WDM states generated in experiments often hinder effective diagnostics. Indeed, one usually has to rely on simulations to extract properties (structural factors, free energy etc.) from the experimental data.

One of the common diagnostic tools in WDM experiments is X-ray Thomson scattering (XRTS) [10], which provides information about the dynamical structure factor of the electrons  $S(\mathbf{q}, \omega)$ . To describe the XRTS signal and, in this way, extract the maximum amount of information about the dynamic properties of WDM, one needs accurate simulation results for  $S(\mathbf{q}, \omega)$ . By virtue of the fluctuation–dissipation theorem connecting  $S(\mathbf{q}, \omega)$  with the dynamical linear density response function [11], agreement between experiment and theory for the XRTS signal can provide reliable access to a great variety of dynamical properties such as the dynamical dielectric function, conductivity, and energy loss characteristics. Furthermore, accurate simulations can be used to guide and design future experiments. This is particularly impor-

tant for highly challenging tasks like the development of inertial confinement fusion (ICF) technology.

Commonly used *ab initio* methods for the computation of the dynamical structure factor are linear-response time-dependent density functional theory (LR-TDDFT) and real-time time-dependent density functional theory (RT-TDDFT) [12], which is formally equivalent in the linear-response regime to LR-TDDFT [13]. More recently, the imaginary time density–density correlation function [a two-sided Laplace transform of  $S(\mathbf{q}, \omega)$ ] that can, in principle, be computed from highly accurate quantum Monte Carlo (QMC) methods has been brought forward by Dornheim *et al.* [14–17] as a new tool for the investigation of the dynamical properties of WDM in thermodynamic equilibrium and beyond [18]. All of these methods have certain computational bottlenecks with respect to the number of particles within the simulation. This can lead to finite size effects that have to be minimized to increase the accuracy of the results. For example, a too small number of particles clearly leads to errors in the calculations of thermodynamic properties (pressure, energy *etc.*) [19–23] as well as dynamic properties such as dynamic density response function [24, 25].

In this work, we consider finite size effects in the electronic density response function of disordered systems due to the dependence on the positions of the nuclei in a snapshot. This problem vanishes for crystals if the box length is commensurate with the crystal periodicity. In this case, periodic boundary conditions represent a real physical picture of solids. In the high temperature limit, which corresponds to the fully ionized plasma state, the electrons are free and the ions provide a neutralizing background [26, 27]. The finite size effect due to the dependence on the used ionic snapshot is expected to be strong for extended disordered systems with sufficiently strong electron-ion coupling. This is often the case for

\* z.moldabekov@hzdr.de

WDM.

For disordered systems, a standard way to reduce finite size effects is to perform an averaging of the simulation results over different snapshots. Alternatively, one can evaluate the uncertainty due to the snapshot-dependence by investigating the properties of interest at different values of the number of particles. In this work, we analyse the effectiveness of these strategies for WDM by considering the density response function of warm dense hydrogen. We consider the dynamic and static density response function, the Kohn-Sham (KS) response function, and the static exchange-correlation kernel; the latter is the second order variational derivative of the XC functional with respect to the density [28].

Recently, Moldabekov *et al* [29, 30] have presented an approach that allows one to compute the static XC kernel for any available XC functional on any rung of Jacob's ladder [31] without explicitly performing the cumbersome second order functional derivative. The key idea of the method is to compute the density change due to the external static harmonic perturbation. This method was used to quantify the quality of various XC functionals by comparing with exact QMC data for warm dense hydrogen [29, 30] and the uniform electron gas [29, 32–35]. One of the remaining open questions regarding the application of the direct perturbation method for the computation of the static XC kernel had been the excitation of density perturbations at wavenumbers different from the wavenumber of the external harmonic perturbation, which vanishes only in the thermodynamic limit  $N \rightarrow \infty$  (with  $N$  being the number of particles). This is one of the problems considered in this work.

The static XC kernel computed using the direct perturbation approach requires knowledge of the macroscopic static KS response function [30]. Furthermore, for the application of this static XC kernel in LR-TDDFT, one needs information about the macroscopic dynamic KS response function. Therefore, an open question is how to average the KS response function over different snapshots. The naive way is to perform arithmetic averaging over the KS response functions of individual snapshots. Here we show that this does not follow from the formal definition of the KS response function. This is a consequence of the nonlinear dependence of the linear density response on the KS response function. As a suitable alternative, we present a rigorously derived formula for the proper averaging of the macroscopic dynamic KS response function over snapshots.

The presented results are relevant not only for the density functional theory (DFT) of WDM, but also for the other simulation methods of WDM, such as QMC [36, 37]. Furthermore, the presented analysis of the finite size effects are relevant for the simulations of other disordered systems like liquid metals.

In the next section II, we present the theory for computing the averaged density response properties and the corresponding formulation of an LR-TDDFT based calculation scheme of the macroscopic density response

function. The simulation details are provided in Sec. III. The application of the developed computational scheme is demonstrated in Sec. IV for the example of warm dense hydrogen. We conclude the paper by summarizing the results and providing an outlook in Sec. V.

## II. THEORY

We consider LR-TDDFT with an adiabatic exchange–correlation kernel. One of the commonly used approximations for a static XC kernel is the adiabatic local density approximation (ALDA). For extended systems, the approach based on the explicit implementation of the second order functional derivative of an XC functional with respect to the density is currently restricted to the ALDA and adiabatic generalized gradient approximation (AGGA). In contrast, the direct perturbation approach is capable of computing the static (adiabatic) XC kernel for any available XC functional from LDA all the way across Jacob's Ladder to hybrid XC functionals [29, 32, 33].

In this section, we first consider the direct perturbation approach to compute the static XC kernel. For this purpose, the static density response function and the static KS response function must be computed by comparing the perturbed and unperturbed density and KS potential values, respectively. Therefore, we discuss how the averaging over snapshots is performed for these quantities. After that, we discuss the LR-TDDFT approach to disordered systems with an adiabatic exchange–correlation kernel. We provide a scheme for the computation of the dynamic macroscopic KS response function in LR-TDDFT that represents a properly averaged value over snapshots. We show that it is not equivalent to the arithmetic mean of the KS response functions computed for separate snapshots. Using a consistent scheme for the averaging, we discuss how a dynamic macroscopic KS response function can be combined with the static XC kernel from the direct perturbation approach to compute the dynamic macroscopic density response function.

### A. The direct perturbation approach

#### A.1. Static total density response to a bare external perturbing field

To obtain the static density response function  $\chi(\mathbf{q}) = \chi(\mathbf{q}, \omega = 0)$ , we perform two sets of KS-DFT simulations. First, we find equilibrium density values of electrons in the field of the ions (the unperturbed system) and then we repeat the simulation, applying an extra static harmonic field (the perturbed system). The corresponding Hamiltonian reads

$$\hat{H}_{\mathbf{q},A} = \hat{H}_e + 2A \sum_{j=1}^N \cos(\mathbf{q} \cdot \hat{\mathbf{r}}_j) , \quad (1)$$

where  $\hat{H}_e$  is the Hamiltonian of the unperturbed system, and  $A$  and  $\mathbf{q}$  being the amplitude and the wavevector of the external perturbation.

In the case of the unperturbed system ( $A = 0$ ), the density distribution of the electrons  $n_{A=0}^i(\mathbf{r})$  for a given spatial configuration of ions is not uniform (with  $i$  being the label of a particular snapshot), i.e.  $n_{A=0}^i(\mathbf{r}) \neq n_0 = \text{const}$ , where  $n_0$  is the mean value of the density. In contrast to crystals, the density distributions for different ionic snapshots are not equivalent for disordered systems. Indeed, the averaged value of the density distribution tends to a constant for a large number of snapshots  $N_s$

$$\langle n_e(\mathbf{r}) \rangle_{A=0} = \lim_{N_s \rightarrow \infty} \frac{1}{N_s} \sum_{i=1}^{N_s} n_{A=0}^i(\mathbf{r}) = n_0. \quad (2)$$

Physically, the homogeneity of disordered systems means that diagnostics (e.g. XRTS) is performed on a macroscopic sample, which has properties independent of the probing direction.

The application of the external harmonic field according to Eq. (1) leads to the density perturbation

$$\Delta n_{\mathbf{q},A}^i(\mathbf{r}) = n_A^i(\mathbf{r}) - n_{A=0}^i(\mathbf{r}). \quad (3)$$

If the perturbation amplitude  $A$  is small enough, the non-linear response can be neglected [38–40] and  $\Delta n_{\mathbf{q},A}^i(\mathbf{r})$  can be described by linear response theory (LRT). Due to periodic boundary conditions, the density perturbation can be written as a Fourier series. Since a cosine perturbation is applied in Eq. (1), here we use a Fourier cosine series,

$$\Delta n_{\mathbf{q},A}^i(\mathbf{r}) = 2 \sum_{\mathbf{G}} \rho_{\mathbf{G}}^i(\mathbf{q}) \cos((\mathbf{q} + \mathbf{G}) \cdot \mathbf{r}), \quad (4)$$

where  $\mathbf{G}$  is the reciprocal lattice vector and the factor two is conventional (cf. the perturbation term in Eq. (1)).

In the case of a harmonic perturbation of a uniform system—such as the uniform electron gas—the density perturbation has the same wavenumber as the external harmonic perturbation, i.e., only  $\rho_{\mathbf{G}=0}^i(\mathbf{q})$  is non-zero [38, 41]. Similarly, after averaging over snapshots, only the term with  $\mathbf{G} = 0$  should survive for disordered systems,

$$\begin{aligned} \Delta n(\mathbf{r})_{\mathbf{q},A} &= \lim_{N_s \rightarrow \infty} \frac{1}{N_s} \sum_{i=1}^{N_s} \Delta n_{\mathbf{q},A}^i(\mathbf{r}) \\ &= 2 \left( \lim_{N_s \rightarrow \infty} \frac{1}{N_s} \sum_{i=1}^{N_s} \rho_{\mathbf{G}=0}^i(\mathbf{q}) \right) \cos(\mathbf{q} \cdot \mathbf{r}) \\ &= 2 \langle \rho(\mathbf{q}) \rangle_{\mathbf{G}=0} \cos(\mathbf{q} \cdot \mathbf{r}), \end{aligned} \quad (5)$$

and all terms with  $\mathbf{G} \neq 0$  vanish after averaging,

$$\langle \rho(\mathbf{q}) \rangle_{\mathbf{G} \neq 0} = \lim_{N_s \rightarrow \infty} \frac{1}{N_s} \sum_{i=1}^{N_s} \rho_{\mathbf{G} \neq 0}^i(\mathbf{q}) = 0. \quad (6)$$

The validity of Eq. (2), Eq. (5), and Eq. (6) is demonstrated numerically in Sec. IV for the example of warm dense hydrogen by computing the averaged values of the unperturbed and perturbed density.

The density response function relates the density perturbation to the external harmonic perturbation in a linear fashion,

$$\rho_{\mathbf{G}}^i(\mathbf{q}) = 2A \cos(\mathbf{q} \cdot \mathbf{r}) \chi_{\mathbf{G}}^i(\mathbf{q}). \quad (7)$$

Using  $\Delta n_e(\mathbf{r})_{\mathbf{q},A}$  from Eq. (5) and Eq. (7), we can write

$$\Delta n(\mathbf{r})_{\mathbf{q},A} = 2A \cos(\mathbf{q} \cdot \mathbf{r}) \frac{1}{N_s} \sum_{i=1}^{N_s} \chi_{\mathbf{G}=0}^i(\mathbf{q}). \quad (8)$$

Therefore, one can compute the macroscopic static linear density response function  $\chi(\mathbf{q})$  of a disordered system (that is homogeneous on average) according to the relation

$$\Delta n(\mathbf{r})_{\mathbf{q},A} = 2A \cos(\mathbf{q} \cdot \mathbf{r}) \chi(\mathbf{q}), \quad (9)$$

where

$$\chi(\mathbf{q}) = \frac{1}{N_s} \sum_{i=1}^{N_s} \chi_{\mathbf{G}=0}^i(\mathbf{q}). \quad (10)$$

As follows from Eq. (10), one can compute  $\chi(\mathbf{q})$  using the density perturbation values computed for individual snapshots,

$$\chi(\mathbf{q}) = \frac{1}{N_s} \sum_{i=1}^{N_s} \frac{\rho_{\mathbf{G}=0}^i(\mathbf{q})}{A} = \frac{\langle \rho(\mathbf{q}) \rangle_{\mathbf{G}=0}}{A}. \quad (11)$$

From Eq. (6), it follows that, on average, one has

$$\lim_{N_s \rightarrow \infty} \frac{1}{N_s} \sum_{i=1}^{N_s} \frac{\rho_{\mathbf{G} \neq 0}^i(\mathbf{q})}{A} = \lim_{N_s \rightarrow \infty} \frac{1}{N_s} \sum_{i=1}^{N_s} \chi_{\mathbf{G} \neq 0}^i(\mathbf{q}) = 0. \quad (12)$$

### A.2. Static KS response function from the direct perturbation method

In the case of the unperturbed system with  $A = 0$ , the KS potential for a given snapshot of ionic positions is inhomogeneous, i.e.  $v_{\text{KS}, A=0}^i(\mathbf{r}) \neq \text{const}$ . Similarly to the electron density, the inhomogeneity in the KS potentials of different snapshots vanishes upon averaging over snapshots. In the limit of an infinite number of snapshots  $N_s$ , the mean value of the KS potential becomes a constant,

$$\langle v_{\text{KS}}(\mathbf{r}) \rangle_{A=0} = \lim_{N_s \rightarrow \infty} \frac{1}{N_s} \sum_{i=1}^{N_s} v_{\text{KS}, A=0}^i(\mathbf{r}) = v_{\text{KS}}^0. \quad (13)$$

For a given snapshot  $i$ , the static cosine perturbation in Eq. (1) leads to the perturbation of the KS potential

$$\Delta v_{\text{KS},A}^i(\mathbf{r}) = v_{\text{KS},A}^i(\mathbf{r}) - v_{\text{KS},A=0}^i(\mathbf{r}), \quad (14)$$

which we represent using a Fourier cosine series,

$$\Delta v_{\text{KS},A}^i(\mathbf{r}) = 2 \sum_{\mathbf{G}} u_{\mathbf{G}}^i(\mathbf{q}) \cos((\mathbf{q} + \mathbf{G}) \cdot \mathbf{r}). \quad (15)$$

Based on the same reasoning as for the electron density, we can write for the averaged value of the perturbation of the KS potential

$$\begin{aligned} \Delta v_{\text{KS}}(\mathbf{r})_{\mathbf{q},A} &= \lim_{N_s \rightarrow \infty} \frac{1}{N_s} \sum_{i=1}^{N_s} \Delta v_{\text{KS},A}^i(\mathbf{r}) \\ &= 2 \left( \lim_{N_s \rightarrow \infty} \frac{1}{N_s} \sum_{i=1}^{N_s} u_{\mathbf{G}=0}^i(\mathbf{q}) \right) \cos(\mathbf{q} \cdot \mathbf{r}) \\ &= 2 \langle u(\mathbf{q}) \rangle_{\mathbf{G}=0} \cos(\mathbf{q} \cdot \mathbf{r}), \end{aligned} \quad (16)$$

where  $u_{\mathbf{G}=0}^i(\mathbf{q})$  is the Fourier component of the KS potential perturbation at  $\mathbf{G} = 0$ .

The static KS response function defines the response of the electron density to a change of the KS potential [42]. Using averaged values  $\Delta n_{\mathbf{q},A}(\mathbf{r})$  from Eq. (5) and  $\Delta v_{\text{KS}}(\mathbf{r})_{\mathbf{q},A}$  from Eq. (16), the static KS response function connecting the average electron density change and the average KS potential perturbation follows from the relation

$$\Delta n_{\mathbf{q},A}(\mathbf{r}) = \chi_{\text{KS}}(\mathbf{q}) \Delta v_{\text{KS}}(\mathbf{r})_{\mathbf{q},A}. \quad (17)$$

From Eq. (17) we find

$$\chi_{\text{KS}}(\mathbf{q}) = \frac{\langle \rho(\mathbf{q}) \rangle_{\mathbf{G}=0}}{\langle u(\mathbf{q}) \rangle_{\mathbf{G}=0}} = \frac{\sum_{i=1}^{N_s} \rho_{\mathbf{G}=0}^i(\mathbf{q})}{\sum_{i=1}^{N_s} u_{\mathbf{G}=0}^i(\mathbf{q})}. \quad (18)$$

Eq. (18) provides the macroscopic static KS response function connecting the average value of the electron density perturbation to the average value of the perturbation of the KS potential over atomic snapshots.

One of the conclusions following from Eq. (18) is that a direct average over KS response functions computed for individual snapshots is not a consistent way to deal with finite size effects. Indeed, one can formally compute the static KS response function for an individual snapshot as

$$\chi_{\text{KS},\mathbf{G}}^i(\mathbf{q}) = \frac{\rho_{\mathbf{G}}^i(\mathbf{q})}{u_{\mathbf{G}}^i(\mathbf{q})}, \quad (19)$$

and define the average value of the macroscopic KS response function as

$$\langle \chi_{\text{KS}}(\mathbf{q}) \rangle = \frac{1}{N_s} \sum_{i=1}^{N_s} \chi_{\text{KS},\mathbf{G}=0}^i(\mathbf{q}). \quad (20)$$

We observe that, in general, if  $n_{A=0}^i(\mathbf{r}) \neq n_0$  and  $v_{\text{KS},A=0}^i(\mathbf{r}) \neq v_{\text{KS}}^0$  for any snapshot, then  $\chi_{\text{KS},\mathbf{G}}^i(\mathbf{q})$  defined by Eq. (18) and  $\langle \chi_{\text{KS}}(\mathbf{q}) \rangle$  from Eq. (20) are not equivalent,

$$\begin{aligned} \frac{\sum_{i=1}^{N_s} \rho_{\mathbf{G}=0}^i(\mathbf{q})}{\sum_{i=1}^{N_s} u_{\mathbf{G}=0}^i(\mathbf{q})} &\neq \frac{1}{N_s} \sum_{i=1}^{N_s} \frac{\rho_{\mathbf{G}=0}^i(\mathbf{q})}{u_{\mathbf{G}=0}^i(\mathbf{q})} \\ &\Downarrow \\ \chi_{\text{KS}}(\mathbf{q}) &\neq \langle \chi_{\text{KS}}(\mathbf{q}) \rangle. \end{aligned} \quad (21)$$

In a strict mathematical sense, the inequality (21) is valid for any system that is not a perfect crystal (defect-free crystal). This includes disordered systems such as warm dense matter and fluids. Moreover, the inequality (21) applies for solids with a large enough number of defects so that different snapshots are not equivalent.

The reason to use Eq. (18) is because it is consistent with the linear response theory formulation for homogeneous systems. In contrast, Eq. (20) results in inconsistency with the standard linear response theory for homogeneous systems. This is demonstrated in Appendix A.

### A.3. Static XC kernel

The static XC kernel based on the averaged values over snapshots of the density and KS potential perturbations can be computed using the density response function  $\chi(\mathbf{q})$  from Eq. (11) and the KS response function  $\chi_{\text{KS}}(\mathbf{q})$  from Eq. (18) [29, 30]:

$$K_{\text{xc}}(\mathbf{q}) = - \left\{ v(q) + \left( \frac{1}{\chi(\mathbf{q})} - \frac{1}{\chi_{\text{KS}}(\mathbf{q})} \right) \right\}. \quad (22)$$

In general, it follows from Eq. (22) that

$$K_{\text{xc}}(\mathbf{q}) \neq \frac{1}{N_s} \sum_{i=1}^{N_s} K_{\text{xc}}^i(\mathbf{q}), \quad (23)$$

where  $K_{\text{xc}}^i(\mathbf{q})$  is computed for an individual snapshot:

$$K_{\text{xc}}^i(\mathbf{q}) = - \left\{ v(q) + \left( \frac{1}{\chi_{\mathbf{G}=0}^i(\mathbf{q})} - \frac{1}{\chi_{\text{KS},\mathbf{G}=0}^i(\mathbf{q})} \right) \right\}. \quad (24)$$

Therefore, a straightforward arithmetic averaging using the static XC kernel for individual snapshots does not provide a consistent result.

The direct perturbation approach and Eq. (22) allow one to compute the static XC kernel for any available XC functional. It was used to compute the static XC kernel of the uniform electron gas and warm dense hydrogen (without averaging over snapshots) using ground state LDA, GGA, and meta-GGA functionals [29, 30] as well as a finite temperature LDA [43] in Ref. [29]. Furthermore, various hybrid XC functionals have been analyzed for the uniform electron gas both in the ground state and at high temperatures in Refs. [32, 33].

## B. LR-TDDFT for disordered systems

### B.1. Dynamic KS response function

We note that  $\chi_{\text{KS},\mathbf{G}=0}^i(\mathbf{q})$  and, in general,  $\chi_{\text{KS},\mathbf{G}=0}^i(\mathbf{q},\omega)$  are well defined for both disordered systems and crystals and represent the macroscopic KS response function following from the macroscopic dielectric function defined within LR-TDDFT [13, 30]. In fact, the static macroscopic KS response function from LR-TDDFT and from the direct perturbation approach are equivalent to each other if the same XC functionals for both methods are used [30]. To extend this equivalence to the dynamic case  $\chi_{\text{KS},\mathbf{G}=0}^i(\mathbf{q},\omega)$ , one needs to use a time-dependent perturbation generating correspondingly time-dependent density and KS potential perturbations in RT-TDDFT, which is outside of the scope of the present work. Nevertheless, LR-TDDFT and RT-TDDFT are formally equivalent in the linear response regime. Therefore, the equivalence of LR-TDDFT and the direct perturbation method is expected to hold for the dynamic case as well if the same XC functional and other parameters are used.

According to the definition of the macroscopic KS response function, we have for disordered systems,

$$\langle \rho(\mathbf{q},\omega) \rangle_{\mathbf{G}=0} = \chi_{\text{KS}}(\mathbf{q},\omega) \langle u(\mathbf{q},\omega) \rangle_{\mathbf{G}=0}, \quad (25)$$

where

$$\langle u(\mathbf{q},\omega) \rangle_{\mathbf{G}=0} = \frac{1}{N_s} \sum_i^{N_s} u_{\mathbf{G}=0}^i(\mathbf{q},\omega), \quad (26)$$

and

$$\langle \rho(\mathbf{q},\omega) \rangle_{\mathbf{G}=0} = \frac{1}{N_s} \sum_i^{N_s} \rho_{\mathbf{G}=0}^i(\mathbf{q},\omega). \quad (27)$$

Therefore, the computation of  $\chi_{\text{KS}}(\mathbf{q},\omega)$  requires information about the dynamic KS potential perturbation ( $u_{\mathbf{G}=0}^i(\mathbf{q},\omega)$ ) and the dynamic density perturbation ( $\rho_{\mathbf{G}=0}^i(\mathbf{q},\omega)$ ), which are not standard outputs of currently available LR-TDDFT codes for extended systems (to our best knowledge). Here we show how to circumvent this problem.

Let us consider the time dependent external perturbation  $\delta V_{\text{ext}}(\mathbf{r},t) = Af(t)\cos(\mathbf{q}\cdot\mathbf{r})$  to access the dynamic density response, where  $f(t)$  is a time dependent function, e.g.,  $f(t)$  can be in the form of a Gaussian envelope [44].

In the LRT, since for the considered cosinoidal potential we have  $\text{Im } \mathcal{F}[\delta V_{\text{ext}}] = 0$  (where  $\mathcal{F}[\dots]$  denotes a Fourier transform), we can use  $\chi_{\mathbf{G}=0}^i(\mathbf{q},\omega)$  to compute  $\text{Re } \rho_{\mathbf{G}=0}^i(\mathbf{q},\omega)$  and  $\text{Im } \rho_{\mathbf{G}=0}^i(\mathbf{q},\omega)$ ,

$$\text{Re } \rho_{\mathbf{G}=0}^i(\mathbf{q},\omega) = \text{Re } \chi_{\mathbf{G}=0}^i(\mathbf{q},\omega) \mathcal{F}[\delta V_{\text{ext}}], \quad (28)$$

$$\text{Im } \rho_{\mathbf{G}=0}^i(\mathbf{q},\omega) = \text{Im } \chi_{\mathbf{G}=0}^i(\mathbf{q},\omega) \mathcal{F}[\delta V_{\text{ext}}]. \quad (29)$$

Eq. (28) and Eq. (29) define  $\rho_{\mathbf{G}=0}^i(\mathbf{q},\omega)$ , which is a complex function. We combine  $\rho_{\mathbf{G}=0}^i(\mathbf{q},\omega)$  with the KS response function  $\chi_{\text{KS},\mathbf{G}=0}^i(\mathbf{q},\omega)$  to find

$$\begin{aligned} u_{\mathbf{G}=0}^i(\mathbf{q},\omega) &= \frac{\rho_{\mathbf{G}=0}^i(\mathbf{q},\omega)}{\chi_{\text{KS},\mathbf{G}=0}^i(\mathbf{q},\omega)} \\ &= \mathcal{F}[\delta V_{\text{ext}}] \frac{\chi_{\mathbf{G}=0}^i(\mathbf{q},\omega)}{\chi_{\text{KS},\mathbf{G}=0}^i(\mathbf{q},\omega)}, \end{aligned} \quad (30)$$

where  $\chi_{\text{KS},\mathbf{G}=0}^i(\mathbf{q},\omega)$  is computed for each snapshot using the LR-TDDFT result for the macroscopic dynamic dielectric function  $\varepsilon_M^{i,\text{RPA}}(\mathbf{q},\omega)$  in the random phase approximation (RPA) (i.e., with zero XC kernel) [30],

$$\chi_{\text{KS},\mathbf{G}=0}^i(\mathbf{q},\omega) = \frac{1}{v(q)} \left( 1 - \varepsilon_M^{i,\text{RPA}}(\mathbf{q},\omega) \right). \quad (31)$$

Finally, using Eqs. (25)-(30), we find

$$\begin{aligned} \chi_{\text{KS}}(\mathbf{q},\omega) &= \frac{\langle \rho(\mathbf{q},\omega) \rangle_{\mathbf{G}=0}}{\langle u(\mathbf{q},\omega) \rangle_{\mathbf{G}=0}} \\ &= \frac{\sum_{i=1}^{N_s} \rho_{\mathbf{G}=0}^i(\mathbf{q},\omega)}{\sum_{i=1}^{N_s} u_{\mathbf{G}=0}^i(\mathbf{q},\omega)} \\ &= \left( \sum_i^{N_s} \chi_{\mathbf{G}=0}^i(\mathbf{q},\omega) \right) \left( \sum_{i=1}^{N_s} \frac{\chi_{\mathbf{G}=0}^i(\mathbf{q},\omega)}{\chi_{\text{KS},\mathbf{G}=0}^i(\mathbf{q},\omega)} \right)^{-1}, \end{aligned} \quad (32)$$

where

$$\chi_{\mathbf{G}=0}^i(\mathbf{q},\omega) = \frac{\chi_{\text{KS},\mathbf{G}=0}^i(\mathbf{q},\omega)}{1 - [v(q) + K_{\text{xc}}^i(q)] \chi_{\text{KS},\mathbf{G}=0}^i(\mathbf{q},\omega)}. \quad (33)$$

Therefore, one needs to compute the KS response function  $\chi_{\text{KS},\mathbf{G}=0}^i(\mathbf{q},\omega)$  using Eq. (19) and the static XC kernel defined by Eq. (24) for each snapshot to find  $\chi_{\text{KS}}(\mathbf{q},\omega)$  using Eq. (32). LR-TDDFT with zero XC kernel delivers  $\chi_{\text{KS},\mathbf{G}=0}^i(\mathbf{q},\omega)$  and the direct perturbation method allows one to compute  $K_{\text{xc}}^i(q)$  for a given snapshot.

As it should be in the linear response regime, the parameters of an external perturbation do not enter Eq. (32). In the case of a perfect crystal—due to use of a primitive cell or a conventional cell—all snapshots are equivalent and we find from Eq. (32) that  $\chi_{\text{KS}}(\mathbf{q},\omega) = \chi_{\text{KS},\mathbf{G}=0}^i(\mathbf{q},\omega)$ , again, as it should be for a macroscopic KS response function of crystal.

In the static limit, Eq. (32) based on the LR-TDDFT gives an equivalent result to Eq. (18) based on the direct perturbation approach.

To the best of our knowledge, the formula (32) for the computation of the macroscopic KS response function that has been averaged properly over snapshots had not been presented in prior works. We stress that  $\chi_{\text{KS}}(\mathbf{q},\omega) \neq \frac{1}{N_s} \sum_{i=1}^{N_s} \chi_{\text{KS},\mathbf{G}=0}^i(\mathbf{q},\omega)$ .



### B.2. LR-TDDFT with adiabatic (static) exchange–correlation kernel

We can now formulate a consistent *adiabatic (static) approximation* for the macroscopic dynamic density response function corresponding to properly averaged values of the density and KS potential perturbations,

$$\chi(\mathbf{q}, \omega) = \frac{\chi_{\text{KS}}(\mathbf{q}, \omega)}{1 - [v(q) + K_{\text{xc}}(\mathbf{q})] \chi_{\text{KS}}(\mathbf{q}, \omega)}, \quad (34)$$

where the dynamic KS response function  $\chi_{\text{KS}}(\mathbf{q}, \omega)$  is given by Eq. (32) and the static XC kernel is defined by Eq. (22).

The dynamic dielectric function that is consistent with Eq. (34) is defined as

$$\varepsilon^{-1}(\mathbf{q}, \omega) = 1 + v(q)\chi(\mathbf{q}, \omega). \quad (35)$$

It is clear that

$$\varepsilon(\mathbf{q}, \omega) \neq \frac{1}{N_s} \sum_i^{N_s} \varepsilon^i(\mathbf{q}, \omega), \quad (36)$$

where  $\varepsilon^i(\mathbf{q}, \omega)$  is the macroscopic dynamic dielectric function of an individual snapshot defined as

$$\frac{1}{\varepsilon^i(\mathbf{q}, \omega)} = 1 + v(q)\chi_{\mathbf{G}=0}^i(\mathbf{q}, \omega). \quad (37)$$

Previously, an adiabatic (static) approximation for the dynamic density response function has been formulated for a given snapshot of ion positions [30]. For the application to disordered systems, we have shown in this work how to overcome finite size effects present in  $\chi_{\mathbf{G}=0}^i(\mathbf{q}, \omega)$  due to the snapshot-dependence by using the averaged values of the density and KS potential perturbations.

We stress that inequality (36) holds for other methods such as RT-TDDFT, where the consistent way is to perform averaging on the level of the density response function and then compute the dielectric function.

### III. SIMULATION DETAILS

For the computation of the static density response and the static KS response function on the basis of the direct perturbation method, we used the ABINIT package [45–50] with the PBE [51] XC functional. The simulations are performed for warm dense hydrogen at  $r_s = 2$  and  $r_s = 4$ , where  $r_s = (4\pi n_0/3)^{-1/3}$  is the mean-interparticle distance and  $n_0$  is the mean number density of electrons (protons). In Ref. [29], it was shown that KS-DFT simulations of hydrogen at the considered WDM parameters provide an accurate description of the static density response by comparing with available quantum Monte Carlo data [36, 37].

We consider ion snapshots with  $N = 14$  and  $N = 112$  particles. In the case of  $N = 14$  particles, results are computed for  $N_s = 10$  different snapshots generated by segmenting a larger ionic configuration that has been obtained from a thermal KS-DFT based molecular dynamics simulations as it is described in Ref. [52]. We consider temperatures corresponding to partial electron degeneracy with  $\theta = T/T_F = 1$ , where  $T_F$  is the Fermi temperature of free electrons. At  $r_s = 2$  ( $r_s = 4$ ), we have  $T \simeq 12.528$  eV ( $T \simeq 3.132$  eV). For the LR-TDDFT calculations of the macroscopic KS response function, we used the GPAW code [53].

For the direct perturbation approach based KS-DFT calculation with  $N = 14$  ( $N = 112$ ) particles in a snapshot, we used  $N_b = 280$  ( $N_b = 2000$ ) bands in the main simulation cell. For  $N = 14$  particles, the k-points sampling was set to  $10 \times 10 \times 10$  with an energy cutoff of 30 Ha. Additionally, for  $r_s = 4$ , we present results for  $N = 378$  particles with  $N_b = 7600$  bands. For  $N = 112$  and  $N = 378$  particles, the k-points sampling was set to  $2 \times 2 \times 2$  with the energy cutoff 30 Ha. The box size for  $N = 14$  ( $N = 112$ ) is  $L = 7.77$  Bohr ( $L = 15.541$  Bohr), which is defined by the relation  $n_0 L^3 = N$ . The amplitude of the external perturbation is set  $A = 0.01$  (in Hartree). It was shown to be within the LRT domain in Ref. [36]. The results are presented in Hartree atomic units.

The convergence of KS-DFT simulations with respect to  $k$ -point grid, energy cutoff, and the number of bands have been studied in [30, 33, 54] for the uniform electron gas (UEG), which has properties similar to fully ionized hydrogen, and warm dense hydrogen [29, 30]. To ensure the convergence of the presented results, in this work, we set same or better computation parameters. For example, the convergence of KS-DFT calculations is tested by reproducing an exact Lindhard response function in the thermodynamic limit in the case of UEG [30]. For warm dense hydrogen, the high-quality of the KS-DFT simulations at considered parameters is tested on the example of LDA XC functional by comparing to the QMC data for the density response [29, 30].

We set  $\mathbf{q}$  along the z-axis. We consider the response of the system along  $\mathbf{q}$  and drop the vector notation for simplicity. The density and KS potential perturbation values are averaged along the  $x$  and  $y$  axes. The perturbation wavenumbers are defined as  $q = j \times q_{\text{min}}$ , where  $q_{\text{min}} = 2\pi/L$  and  $j$  denotes a positive integer number. For  $N = 14$ , we have  $q_{\text{min}}^{N=14} \simeq 0.84268 q_F$ , for  $N = 112$  we have  $q_{\text{min}}^{N=112} \simeq 0.42134 q_F$ , and for  $N = 378$  we have  $q_{\text{min}}^{N=378} \simeq 0.280894 q_F$ . Since  $q_{\text{min}}^{N=14} = 2q_{\text{min}}^{N=112}$  and  $q_{\text{min}}^{N=14} = 3q_{\text{min}}^{N=378}$ , we can compare results computed using  $N = 14$ ,  $N = 112$ , and  $N = 378$  particles.

To demonstrate the application of Eq. (32), LR-TDDFT calculations of the macroscopic dynamic KS response function are performed for  $r_s = 2$  using  $N_s = 10$  different snapshot with  $N = 14$  electrons (protons) in each,  $10 \times 10 \times 10$  k-points, a cutoff in the dielectric function of 100 eV and a broadening parameter  $\eta = 0.2$ .

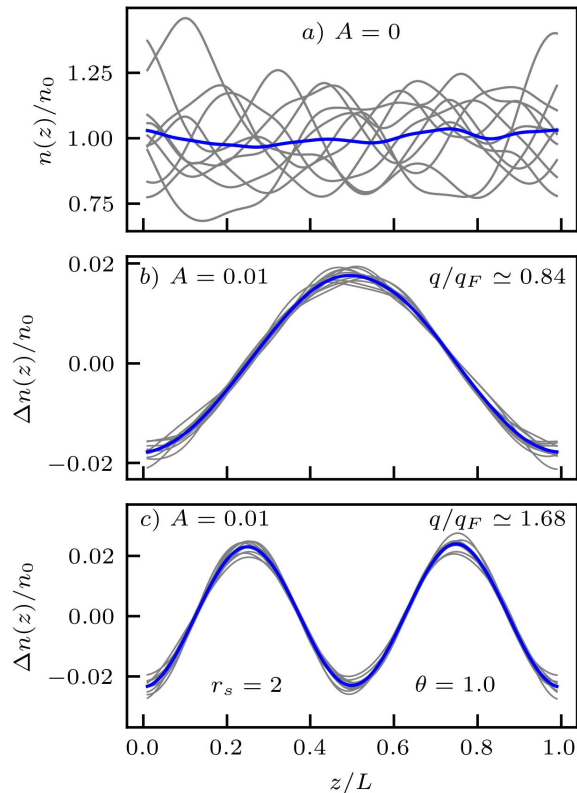


FIG. 1. a) Density distribution along the  $z$  axis of the unperturbed system, b) density perturbation for  $A = 0.01$  and  $q \simeq 0.84q_F$ , and c) density perturbation for  $A = 0.01$  and  $q \simeq 1.68q_F$ . The results are computed for  $r_s = 2$  and  $\theta = 1$ .

#### IV. RESULTS AND DISCUSSIONS

We first present the results for the static density response, static KS response, and static XC kernel computed using the direct perturbation approach and theory presented in Sec. II A. After that, we demonstrate the application of the averaging scheme for the dynamic density response function presented in Sec. II B.

##### A. Static density response and XC kernel

We consider warm dense hydrogen at  $r_s = 2$  and  $r_s = 4$ . The former corresponds to a characteristic metallic density with a high ionization degree and the latter to a partially ionized dense gaseous state consisting of ions and neutral atoms [36, 37, 55]. Therefore, we have stronger electron-ion coupling at  $r_s = 4$  than at  $r_s = 2$  and, correspondingly, a more pronounced degree of inhomogeneity in the electron density for a given snapshot.

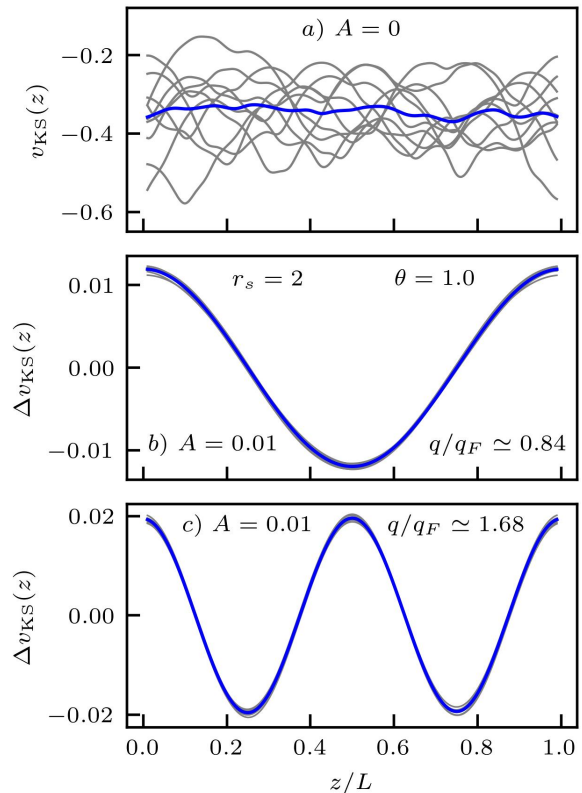


FIG. 2. a) KS potential distribution along the  $z$  axis of the unperturbed system, b) KS potential perturbation for  $A = 0.01$  and  $q \simeq 0.84q_F$ , and c) KS potential perturbation for  $A = 0.01$  and  $q \simeq 1.68q_F$ . The results are computed for  $r_s = 2$  and  $\theta = 1$ .

##### A.1. Hydrogen at metallic density, $r_s = 2$

In Fig. 1, we show the unperturbed electron density as well as the density perturbations due to an external harmonic field for 10 different snapshots (grey curves); the solid blue lines depict the corresponding mean values. From Fig. 1 a), we clearly see that the unperturbed densities are inhomogeneous and that averaging over snapshots leads to a homogeneous density profile. In Fig. 1 b) and Fig. 1 c), we present results for the perturbation wavenumbers  $q = q_{\min}^{N=14} \simeq 0.84268 q_F$  and  $q = 2q_{\min}^{N=14}$ . We observe that averaging leads to a cancellation of the small deviations from the cosinusoidal shape of the density perturbation following the shape of the external perturbation.

In Fig. 2, we present results for the KS potential of the unperturbed and perturbed systems. Similarly to the density distribution, the KS potential profile is inhomogeneous for individual snapshots and tends to the homogeneous distribution upon averaging over snapshots (see Fig. 2 a)). In the case of the perturbed system, the averaged value of the KS potential perturbation, presented in Fig. 2 b) and Fig. 2 c), closely follows the

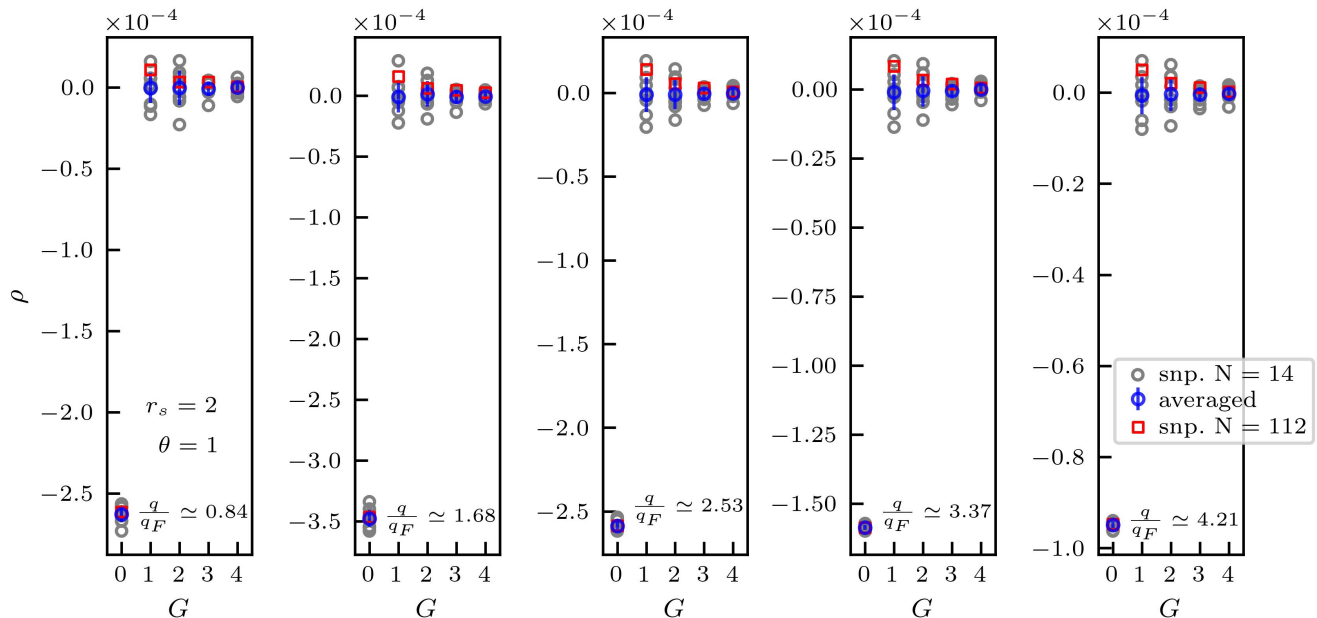


FIG. 3. Contributions to the total density change from density perturbation values at different wave numbers for different snapshots (the grey circles are for 14 particles and red symbols are for 112 particles), and for the averaged values over 10 snapshots with 14 particles (blue circles) in warm dense hydrogen at  $r_s = 2$  and  $\theta = 1$ . The wave number  $q$  corresponds to the wavenumber of the external perturbation. The  $\mathbf{G}$  is along the  $z$ -axis and in units of  $2\pi/L$ .

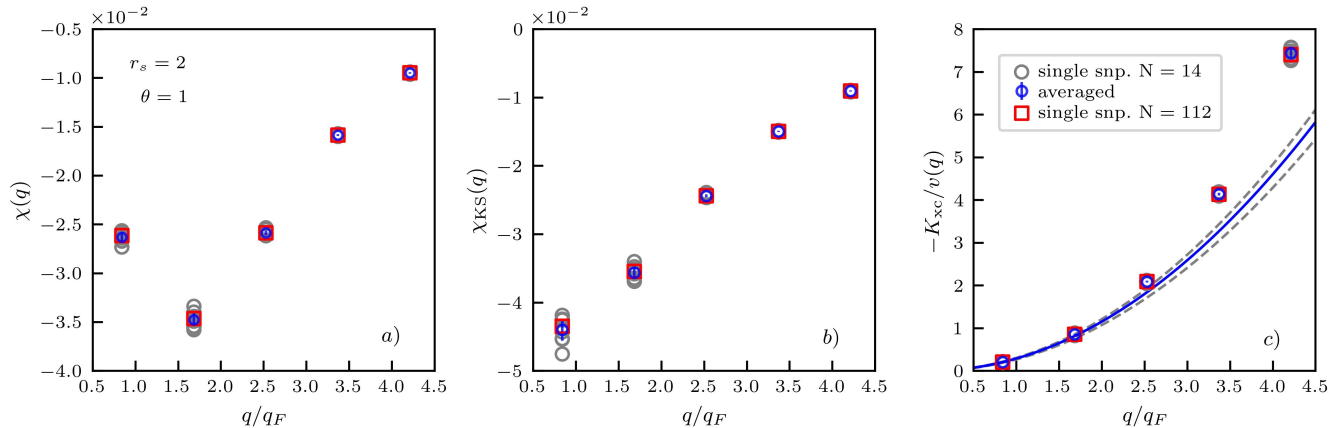


FIG. 4. a) Total static density response function, b) static KS response function, and c) static XC kernel of warm dense hydrogen at  $r_s = 2$  and  $\theta = 1$ . Grey circles are for 14 particles and red squares are for 112 particles. Blue circles are for the averaged values over 10 snapshots with 14 particles.

external perturbation. We note that the deviation of the KS potential perturbation for individual snapshots from the cosinoidal shape is less pronounced compared to the density perturbation profiles at the same parameters (cf. Fig. 1 b) and Fig. 1 c)).

From the results presented in Fig. 1 and Fig. 2, it is clear that averaged values of the density perturbation and KS potential perturbation have a cosinoidal shape with the wavenumber  $q$  being equal to that of the external harmonic field. To further confirm this observa-

tion, we show in Fig. 3 the contributions to the total density change from density perturbation values  $\rho_G(q)$  (computed using Eq. (4)) at different wavenumbers  $G$  and  $q$ . In Fig. 3, we present results for 10 different snapshots of  $N = 14$  particles, for the corresponding averaged values, and for one snapshot with  $N = 112$  particles. Additionally, we show corresponding standard deviations of a single snapshot, which are depicted as “error bars”. From Fig. 3, we see that  $\rho_{G \neq 0}^i(q)$  values for different snapshots have different signs, and have



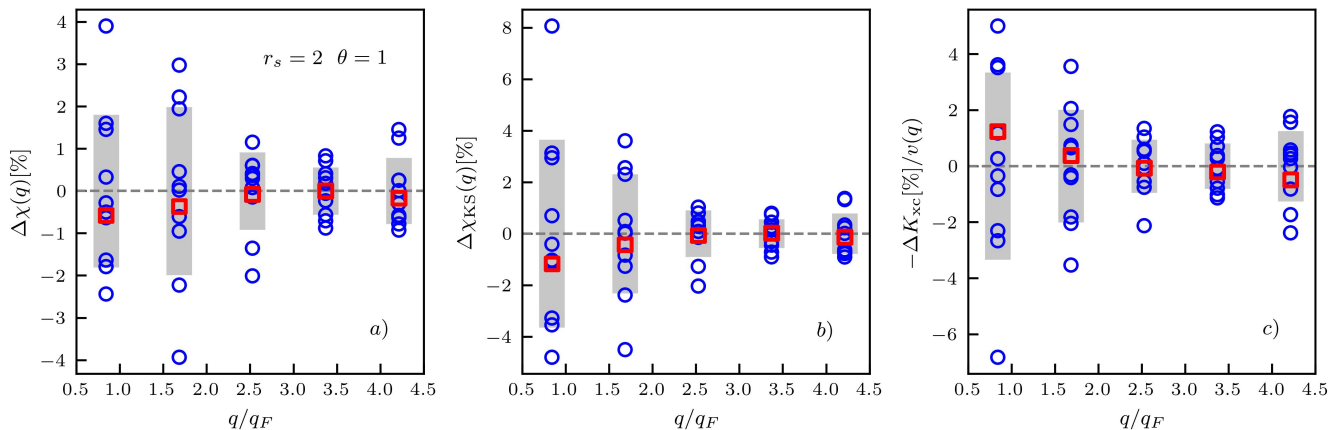


FIG. 5. Difference of a) the total static density response function, b) the static KS response function, and c) the static XC kernel computed for a single snapshot from the corresponding averaged values at  $r_s = 2$  and  $\theta = 1$ . Colored circles are for the snapshots with 14 particles and red symbols are for the snapshot with 112 particles.

magnitudes much less than that of  $\rho_{G=0}^i(q)$ . In contrast, all  $\rho_{G=0}^i(q)$  values for the considered snapshots have the same sign and relatively close values; this is shown numerically below considering density response functions. As a result, we have  $\langle \rho(q) \rangle_{G=0} \gg \langle \rho(q) \rangle_{G \neq 0}$  for the mean values and, compared to the contribution at  $G = 0$ , one can set  $\langle \rho(q) \rangle_{G \neq 0} \approx 0$ . Furthermore, we see that the averaged value  $\langle \rho(q) \rangle_{G=0}$  computed for  $N = 14$  particles is in close agreement with  $\rho_{G=0}^i(q)$  computed for  $N = 112$  particles. In contrast, there are significant disagreements between  $\rho_{G \neq 0}^i(q)$  for a snapshot with  $N = 112$  particles and  $\langle \rho(q) \rangle_{G \neq 0}$  computed by averaging over 10 snapshots with  $N = 14$  particles in each. Additionally, we observe that  $\rho_{G \neq 0}^i(q)$  for the snapshot with  $N = 112$  particles has magnitudes comparable with  $\rho_{G \neq 0}^i(q)$  for a single snapshot with  $N = 14$  particles.

In Fig. 4, we show the results for a) the static density response function, b) the static KS response function, and c) the static XC kernel of warm dense hydrogen at  $r_s = 2$  and  $\theta = 1$ . In Fig. 4 a), the averaged value of the static density response function  $\chi(q)$  is computed using Eq. (11) and the static density response function for an individual snapshot  $\chi_{G=0}^i(q)$  is computed using Eq. (7). As one can see from Fig. 4 a), the  $\chi(q)$  computed for  $N = 14$  particles is in good agreement with  $\chi_{G=0}^i(q)$  computed for  $N = 112$  particles. The standard deviations for snapshots with  $N = 14$  particles are also shown.

In Fig. 4 b), the macroscopic static KS response function  $\chi_{KS}(q)$  characterizing the density response to the change in the KS potential on average is computed using Eq. (18) (presented with corresponding standard deviations of a single snapshot), and the static KS response function for an individual snapshot  $\chi_{KS,G=0}^i(q)$  is computed using Eq. (19). From Fig. 4 b), we see that  $\chi_{KS}(q)$  computed for  $N = 14$  particles is in close agreement with  $\chi_{KS,G=0}^i(q)$  calculated for a snapshot with  $N = 112$  par-

ticles. In contrast, the  $\chi_{KS,G=0}^i(q)$  values obtained using snapshots with  $N = 14$  particles have visible disagreements with the results for  $\chi_{KS}(q)$ .

To analyze the data for the static XC kernel  $K_{xc}(q)$ , we use the so-called local field correction [56]  $-K_{xc}(q)/v(q)$ , which is commonly used for the study of the dielectric properties of homogeneous systems such as quantum Fermi liquids [11] and, in particular, uniform electron gas [22]. We note that the local field correction is not related to the term “local field effects” used in the context of LR-TDDFT to describe the density inhomogeneity induced by the ions. In Fig. 4 c), we present the data for the static XC kernel  $K_{xc}(q)$  computed using Eq. (22). The results for  $K_{xc}(q)$  and the corresponding standard deviations are based on the data generated for  $N_s = 10$  snapshots with  $N = 14$  particles in each of them. We compare the  $K_{xc}(q)$  with the  $K_{xc}^i(q)$  values computed using Eq. (24) for each snapshot separately with  $G = 0$ . Additionally, we compare with the  $K_{xc}^i(q)$  values calculated for one snapshot with  $N = 112$  particles. Additionally, we plot a quadratic dependence accurately describing the local field correction  $-K_{xc}(q)/v(q)$  at  $q \lesssim 1.5q_F$ . The solid (blue) line is obtained using the  $K_{xc}(q)$  value at  $q < q_F$  and the dashed (grey) lines are defined by the smallest and largest values of the  $K_{xc}^i(q)$  (at  $q < q_F$ ) among considered snapshots. From Fig. 4 c), we observe a close agreement between  $K_{xc}(q)$  based on averaged quantities and  $K_{xc}^i(q)$  computed for one snapshot with  $N = 112$  particles. From Fig. 4, we see that the local field corrections  $-K_{xc}(q)/v(q)$  and  $-K_{xc}^i(q)/v(q)$  follow a quadratic behavior at  $q \lesssim 1.5q_F$  and show faster increase than the quadratic dependence with the increase in the wavenumber at  $q > 2q_F$ .

To further quantify the difference between the results for individual snapshots and for the averaged values of the considered density response characteristics, we plot

the relative deviation of  $\chi_{G=0}^i(q)$  from  $\chi(q)$  computed as

$$\Delta\chi(q) = \frac{\chi_{G=0}^i(q) - \chi(q)}{\chi(q)} \times 100\% \quad (38)$$

in Fig. 5a). Further, we show the relative deviation of  $\chi_{\text{KS},G=0}^i(q)$  from  $\chi_{\text{KS}}(q)$ ,

$$\Delta\chi_{\text{KS}}(q) = \frac{\chi_{\text{KS},G=0}^i(q) - \chi_{\text{KS}}(q)}{\chi_{\text{KS}}(q)} \times 100\% , \quad (39)$$

in Fig. 5b), the relative deviation of  $K_{\text{xc}}^i(q)$  from  $K_{\text{xc}}(q)$ ,

$$\Delta K_{\text{xc}}(q) = \frac{K_{\text{xc}}^i(q) - K_{\text{xc}}(q)}{K_{\text{xc}}(q)} \times 100\% , \quad (40)$$

in Fig. 5c). The  $\Delta\chi(q)$ ,  $\Delta\chi_{\text{KS}}(q)$ , and  $\Delta K_{\text{xc}}(q)$  values are shown as blue circles, grey areas represent the standard deviations (of a single snapshot) estimated using  $N_s = 10$  snapshots of  $N = 14$  particles, and red squares depict data computed comparing the results for one snapshot with  $N = 112$  particles to the averaged values based on 10 snapshots with  $N = 14$  particles. From Fig. 5, we see that the disagreement between  $\chi(q)$  computed by averaging over snapshots with  $N = 14$  particles and  $\chi_{G=0}^i(q)$  computed for a single snapshot with  $N = 112$  particles is less than 1%. For  $\chi_{\text{KS}}(q)$  and  $K_{\text{xc}}(q)$ , the disagreement with  $\chi_{\text{KS},G=0}^i(q)$  and  $K_{\text{xc}}^i(q)$  of the snapshot with  $N = 112$  particles, is less than about 1.5%. These deviations for the averaged values with  $N = 14$  particles and the values obtained for a single snapshot with  $N = 112$  particles are significantly smaller than the standard deviations evaluated using  $N_s = 10$  snapshots of  $N = 14$  particles. In contrast, results for  $\chi_{G=0}^i(q)$ ,  $\chi_{\text{KS},G=0}^i(q)$  and  $K_{\text{xc}}^i(q)$  for the snapshots with  $N = 14$  particles deviate from the corresponding averaged values by up to about 4%, 8%, and 7%, respectively.

### A.2. Partially ionized dense hydrogen, $r_s = 4$

At  $r_s = 4$ , we have a stronger coupling between electrons and ions compared to the case with  $r_s = 2$ . This means that electrons are localised around ions to a larger degree. This can be seen from Fig. 6 a), where density profiles for  $N_s = 10$  different snapshots with  $N = 14$  particles (solid grey lines) are shown for the unperturbed dense hydrogen gas at  $r_s = 4$  and  $\theta = 1$  ( $T \simeq 3.132$  eV). From Fig. 6 a), we see that the density values deviate from the mean density  $n_0$  by up to 100%. Nevertheless, the averaged value over snapshots of the equilibrium density is homogeneous (solid blue line) due to the disordered structure at the considered parameters. In the case of the perturbed system presented in Fig. 6b) and Fig. 6c), the density averaging over 10 snapshots effectively eliminates the deviations from the cosinoidal profile in the density perturbation. This is also demonstrated for snapshots with 112 particles in the Appendix B.

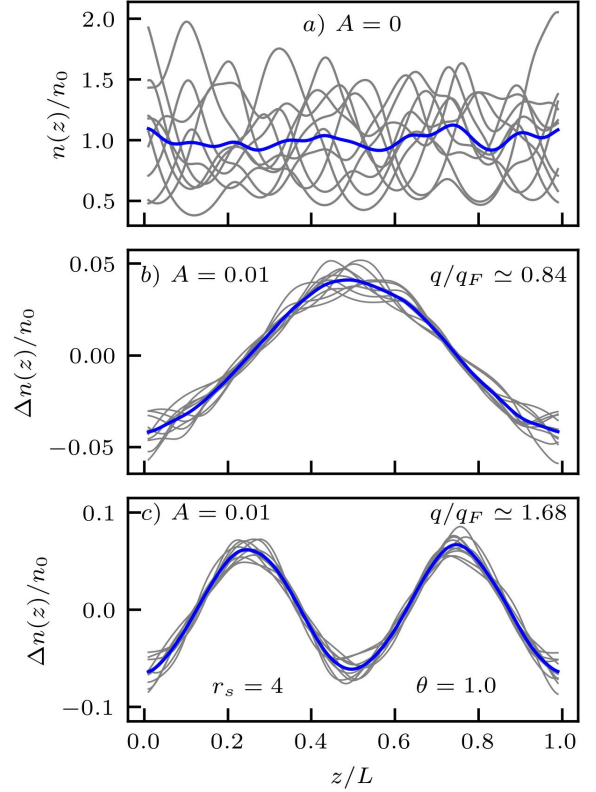


FIG. 6. a) Density distribution along the  $z$  axis of the unperturbed system, b) density perturbation at  $A = 0.01$  and  $q \simeq 0.84q_F$ , and c) density perturbation at  $A = 0.01$  and  $q \simeq 1.68q_F$ . The results are computed for  $r_s = 4$  and  $\theta = 1$ .

In Fig. 7, we show the KS potential profiles for the unperturbed system and for the perturbed system with  $r_s = 4$  and  $\theta = 1$ . We see that the KS potential for individual snapshots (with  $N = 14$  particles) is strongly inhomogeneous. These inhomogeneities are smoothed out after averaging over snapshots and the KS potential distribution becomes nearly uniform due to disordered structure of the system. In the perturbed systems shown in Fig. 7b) and Fig. 7c), the KS potential distribution follows the external perturbation. The deviations from the cosinoidal distribution are visible for individual snapshots. These deviations are diminished significantly by averaging over snapshots.

To further demonstrate that only a single Fourier component at the wavenumber of the external harmonic perturbation remains after averaging of the density perturbations over snapshots, we present the density perturbation values  $\rho_G(q)$  (as defined in Eq. (4)) at different  $G$  and  $q$  values in Fig. 8. We find that the  $\rho_{G \neq 0}(q)$  components have significant contributions for individual snapshots, but with different signs. The latter leads to the mutual cancellation of the  $\rho_{G \neq 0}(q)$  values from different snapshots after averaging. In the Appendix B, we also demonstrate it for snapshots with 112 particles. In con-

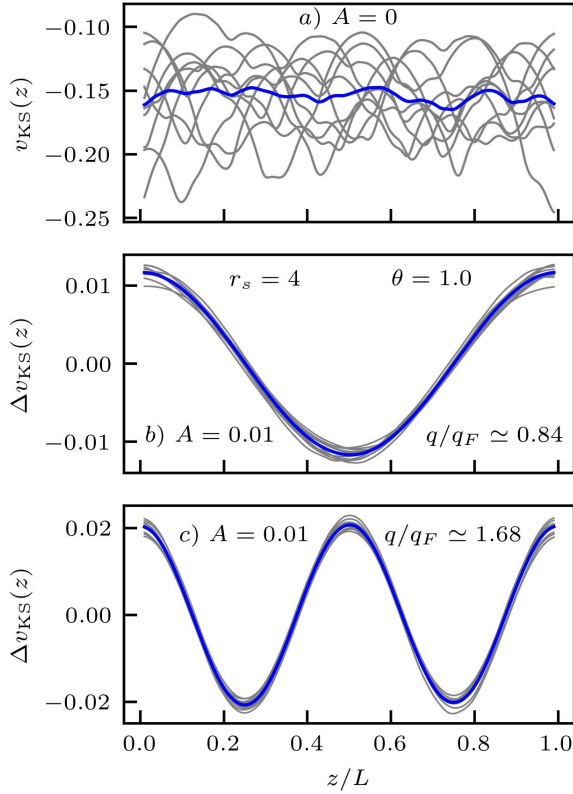


FIG. 7. a) KS potential distribution along the  $z$  axis of the unperturbed system, b) KS potential perturbation at  $A = 0.01$  and  $q \simeq 0.84q_F$ , and c) KS potential perturbation at  $A = 0.01$  and  $q \simeq 1.68q_F$ . The results are computed for  $r_s = 4$  and  $\theta = 1$ .

trast, the  $\rho_{G=0}(q)$  components of different snapshots have the same sign and after averaging over snapshots we have  $\langle \rho(q) \rangle_{G=0} \gg \langle \rho(q) \rangle_{G \neq 0}$ , and, comparing with  $\langle \rho(q) \rangle_{G=0}$ , one can safely neglect  $\langle \rho(q) \rangle_{G \neq 0}$ . Additionally, we observe that, in general, the  $\langle \rho(q) \rangle_{G=0}$  values computed by averaging over  $N_s = 10$  snapshots of  $N = 14$  particles are in a good agreement with the  $\rho(q)_{G=0}^i$  values obtained using a single snapshot of  $N = 112$  or  $N = 378$  particles.

Next, we show in Fig. 9 results for a) the density response functions, b) the KS response functions, and for c) the static XC kernels computed for  $N_s = 10$  snapshots of  $N = 14$  particles, averaged values over these snapshots, and for a single snapshot with  $N = 112$  particles. From Fig. 9, we see that the averaged values are in good agreement with the data computed using one snapshot of  $N = 112$  particles. In contrast, we find that  $\chi_{G=0}^i(q)$  and  $\chi_{KS,G=0}^i(q)$  of the snapshots with  $N = 14$  particles deviate significantly from the corresponding averaged values at  $q \lesssim 3q_F$ . We observe similar trends for the static XC kernel at  $q \gtrsim 3q_F$ .

In Fig. 9 c), we also show a quadratic approximation for the local field correction  $-K_{xc}(q)/v(q)$ . The solid (blue) line is computed using the  $K_{xc}(q)$  value at

$q < q_F$  and the dashed (grey) lines correspond to the smallest and largest values of the  $K_{xc}^i(q)$  (at  $q < q_F$ ) among the considered snapshots. From Fig. 9 c), one can see that the XC kernel describing the averaged value is very well described by the quadratic curve at all considered wavenumbers. For individual snapshots, the XC kernel can increase faster or slower than quadratic upon increasing the wavenumber depending on the configuration of ions. This is in contrast to the behavior of the XC kernels computed for  $r_s = 2$ . Therefore, the considered case of  $r_s = 4$  more clearly illustrates the importance of the averaging procedure to reveal the correct trends.

To more clearly analyse the difference between the data for the individual snapshots and the averaged values corresponding to these snapshots, we show  $\Delta\chi(q)$  defined in Eq. (38),  $\Delta\chi_{KS}(q)$  defined in Eq. (39), and  $\Delta K_{xc}(q)$  computed using Eq. (40) in Fig. 10. Additionally, we provide the standard deviations estimated using  $N_s = 10$  snapshots of  $N = 14$  particles (see grey areas).

From Fig. 10, we see that the averaged values of the static density response function, the KS response function, and the static XC kernel obtained using snapshots with  $N = 14$  particles exhibit a disagreement with the results from one snapshot with  $N = 112$  particles of less than 2% (depicted using red squares). In contrast, this difference (blue circles) reaches about 8% for the density response function, about 17% for the KS response function, and about 14% for the static XC kernel for the considered individual snapshots with  $N = 14$  particles.

## B. Dynamic density response function

In order to demonstrate the application of Eq. (18) derived in Sec. IIB for averaging the dynamic KS response function, we present in Fig. 11 the results for the dynamic KS response functions  $\chi_{KS}(q, \omega)$  and  $\chi_{KS,G=0}^i(q, \omega)$ , and dynamic dielectric functions  $\epsilon_{KS}(q, \omega)$  and  $\epsilon_{KS,G=0}^i(q, \omega)$  for  $q/q_F \simeq 0.084$ .

In the top rows of Fig. 11, we show the real and imaginary parts of  $\chi_{KS,G=0}^i(q, \omega)$  (grey lines). For the calculation of  $\chi_{KS,G=0}^i(q, \omega)$  we used Eq. (31). We also show  $\chi_{KS}(q, \omega)$  (blue lines) calculated using data from  $N_s = 250$  snapshots of  $N = 14$  particles according to Eq. (32). For the calculation of  $\chi_{G=0}^i(q, \omega)$ , we used Eq. (33), with the static XC kernel  $K_{xc}^i(q)$  being defined by Eq. (24).

The second row from the top in Fig. 11 shows the normalized difference between the  $\chi_{KS}(q, \omega)$  and the mean arithmetic value  $\langle \chi_{KS}(\mathbf{q}, \omega) \rangle = \frac{1}{N_s} \sum_{i=1}^{N_s} \chi_{KS,G=0}^i(\mathbf{q}, \omega)$ . The normalized difference between the real and imaginary parts of  $\chi_{KS}(q, \omega)$  and  $\langle \chi_{KS}(\mathbf{q}, \omega) \rangle$  are computed as

$$\Delta \text{Re } \chi_{KS} = \frac{\text{Re} \langle \chi_{KS}(\mathbf{q}, \omega) \rangle - \text{Re } \chi_{KS}(q, \omega)}{\max |\text{Re } \chi_{KS}(q, \omega)|} \times 100\%, \quad (41)$$

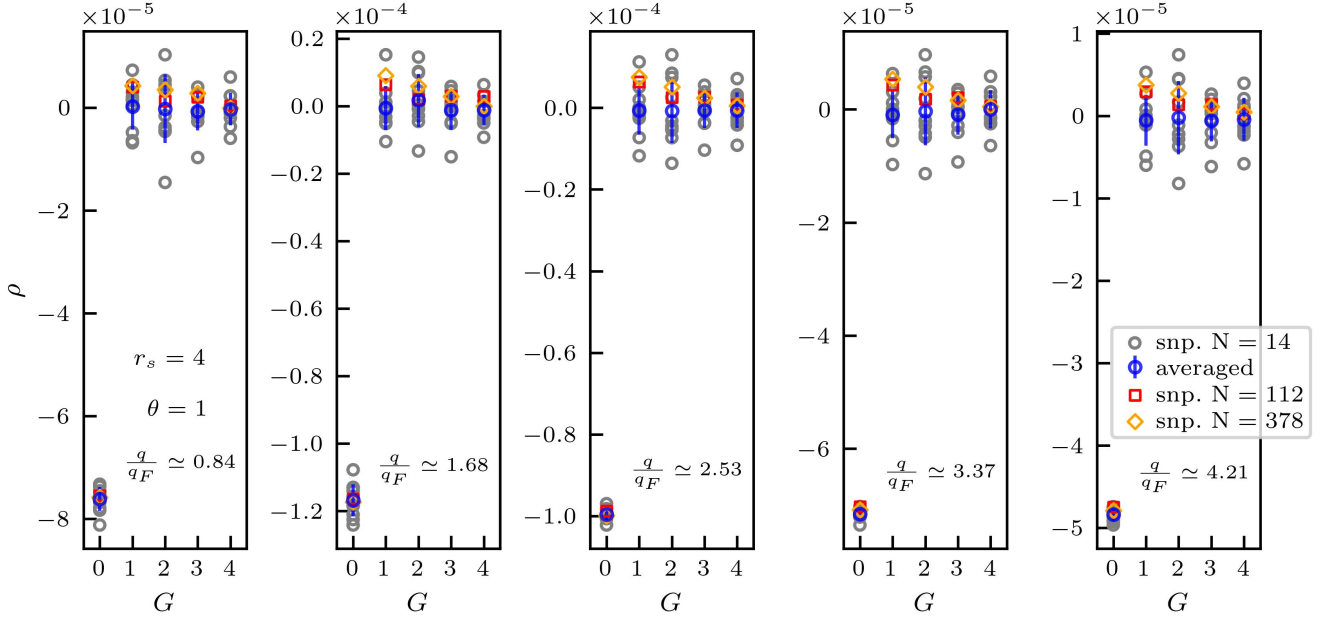


FIG. 8. Contributions to the total density change from the density perturbation values at different wavenumbers for different snapshots (the grey circles are for 14 particles and red (orange) symbols are for 112 (378) particles), and for the averaged values over 10 snapshots with 14 particles (blue circles) in warm dense hydrogen at  $r_s = 4$  and  $\theta = 1$ . The wave number  $q$  corresponds to the wavenumber of the external perturbation. The  $\mathbf{G}$  is along the  $z$ -axis and in units of  $2\pi/L$ .

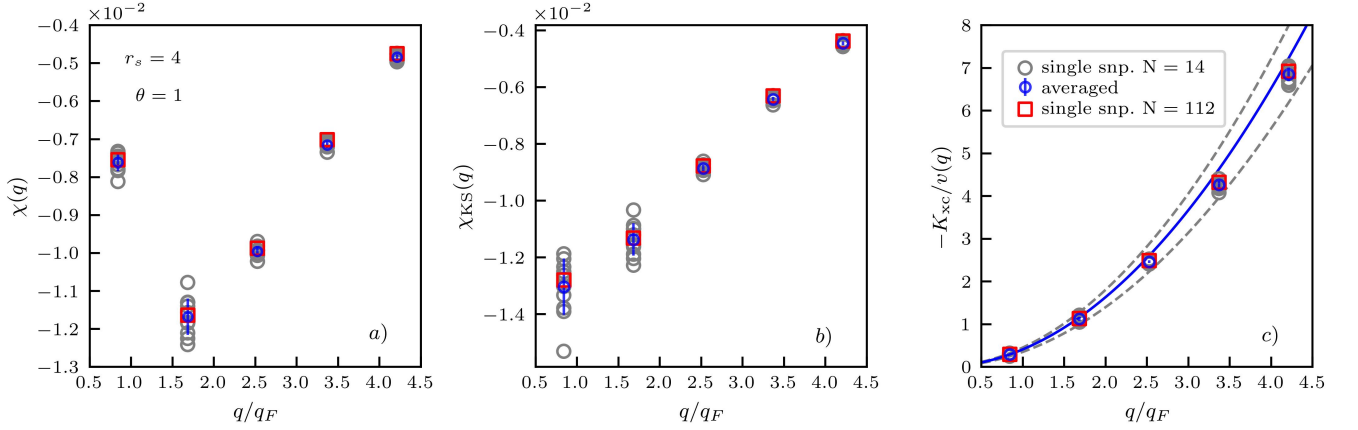


FIG. 9. a) Total static density response function, b) static KS response function, and c) static XC kernel of warm dense hydrogen at  $r_s = 4$  and  $\theta = 1$ . Grey circles are for 14 particles and red squares are for 112 particles. Blue circles are for the averaged values over 10 snapshots with 14 particles.

and

$$\Delta \text{Im } \chi_{\text{KS}} = \frac{\text{Im} \langle \chi_{\text{KS}}(\mathbf{q}, \omega) \rangle - \text{Im } \chi_{\text{KS}}(q, \omega)}{\max |\text{Im } \chi_{\text{KS}}(q, \omega)|} \times 100\%. \quad (42)$$

The third row from the top corresponds to the real and imaginary parts of the dynamic dielectric functions  $\varepsilon(q, \omega)$  (blue lines) and  $\varepsilon^i(q, \omega)$  (grey lines); with  $\varepsilon^i(q, \omega)$  being defined by Eq. (37). To find  $\varepsilon(q, \omega)$  according to Eq. (35), we calculated the averaged value  $\chi(q, \omega)$  by combining  $\chi_{\text{KS}}(q, \omega)$  with  $K_{\text{xc}}(q)$  (defined by Eq. (22))

using Eq. (34).

Finally, the bottom rows shows the the normalized difference between the real and imaginary parts of the  $\varepsilon(q, \omega)$  and the mean arithmetic value  $\langle \varepsilon(q, \omega) \rangle = \frac{1}{N_s} \sum_{i=1}^{N_s} \varepsilon^i(q, \omega)$  computed as

$$\Delta \text{Re } \varepsilon = \frac{\text{Re} \langle \varepsilon(q, \omega) \rangle - \text{Re } \varepsilon(q, \omega)}{\max |\text{Re } \varepsilon(q, \omega)|} \times 100\%, \quad (43)$$



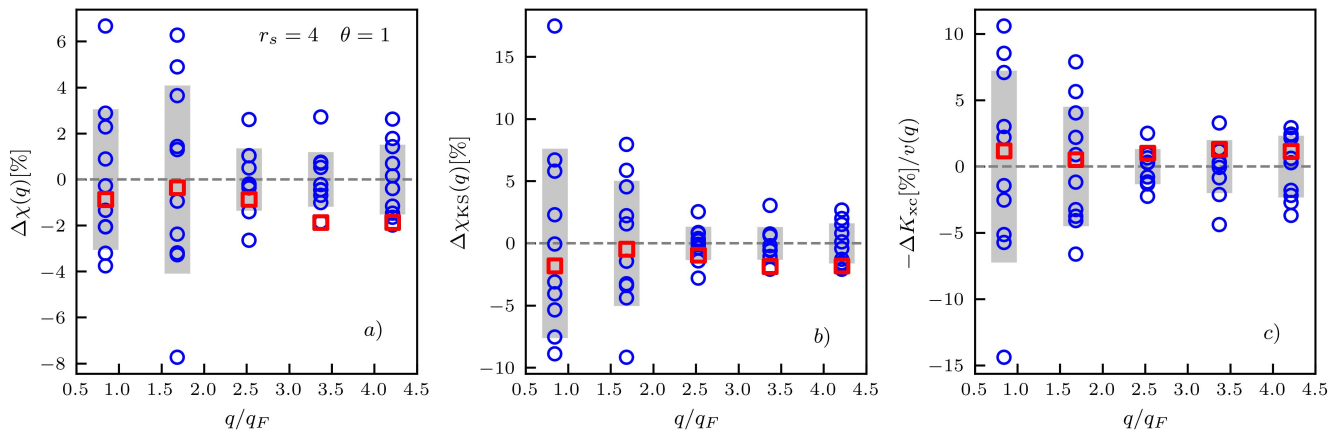


FIG. 10. Difference of a) the total static density response function, b) the static KS response function, and c) the static XC kernel computed for a single snapshot from the corresponding averaged values at  $r_s = 2$  and  $\theta = 1$ . Colored circles are for the snapshots with 14 particles and red symbols are for a snapshot with 112 particles.

and

$$\Delta \text{Im } \varepsilon = \frac{\text{Im} \langle \varepsilon(q, \omega) \rangle - \text{Im } \varepsilon(q, \omega)}{\max |\text{Im } \varepsilon(q, \omega)|} \times 100\%. \quad (44)$$

From Fig. 11, we see that the  $\Delta \text{Re } \chi_{\text{KS}}$  and  $\Delta \text{Re } \varepsilon$  values reach up to about 1% at  $q/q_F \simeq 0.084$ . For the  $\Delta \text{Im } \chi_{\text{KS}}$  and  $\Delta \text{Im } \varepsilon$ , we found the largest deviation values about 2%. We note that the standard error ( a standard deviation divided by  $\sqrt{N_s}$ ) is smaller than the observed values of the difference of the results obtained using different averaging formulas. This dependence on the averaging formulas diminishes with the increase in the wavenumber as it is illustrated in Appendix V for  $q/q_F \simeq 0.758$ . This makes intuitive sense as smaller values of  $q$  correspond to the probing of larger length, leading to an increase in finite-size effects without proper averaging.

In general, it is clear that the values of the errors due to an inconsistent averaging over snapshots depend on the characteristics of the system under consideration and can be both smaller or larger than that of in the considered example of partially degenerate warm dense hydrogen. The usage of the presented averaging workflow allows one to eliminate this unnecessary uncertainty.

## V. CONCLUSIONS AND OUTLOOK

We have presented a consistent scheme for the computation of the properly averaged macroscopic dynamic dielectric function and KS response function. We used the adiabatic (static) approximation to  $\chi(q, \omega)$ , which is based on the static XC kernel calculation method developed recently in Refs. [29, 30] using the direct perturbation approach. The strength of this method is that it allows one to compute the static XC kernel for any available XC functional.

For disordered systems, the dynamic density response function and dynamic dielectric function depend on the positions of ions in the used snapshot. This dependence, together with periodic boundary conditions, represents a finite size effect since in the extended macroscopic disordered systems a structure of ions (atoms) does not have periodicity as in crystals. Since the size of the main simulation cell is proportional to the inverse cube root of the number of particles in it, the increase in the number of particles is not an effective strategy for computationally expensive *ab initio* simulation methods like thermal KS-DFT (particularly at high temperatures [52]), the generalized KS-DFT employing hybrid XC functionals [32, 33, 57–59], and quantum Monte Carlo methods [22]. Alternatively, one can perform averaging over snapshots to diminish this finite size effect. We have demonstrated that this can be an effective strategy on the example of warm dense hydrogen using  $N_s = 10$  snapshots of  $N = 14$  particles.

Furthermore, considering an external perturbation with a wavenumber  $\mathbf{q}$ , we have shown that the induced density and KS potential excitations at  $\mathbf{q} + \mathbf{G}$  (where  $\mathbf{G} \neq 0$ ) disappear after averaging over snapshots. Therefore, we have demonstrated that a sufficiently weak external harmonic perturbation induces the linear density response only at the same wavenumber  $\mathbf{q}$  as that of the external harmonic field for disordered systems. If one increases the amplitude of the perturbing field, the response of the system becomes non-linear [38–40]. This is known to be manifested by the appearance of the density excitations at higher harmonics  $2q$  (for the quadratic response),  $3q$  (for the cubic response) etc. In a recent paper by Böhme *et al* [36], it was shown for warm dense hydrogen using quantum Monte Carlo simulations (at parameters similar to those considered in this work), that it is problematic to resolve a non-linear excitations at different harmonics for a single snapshot with 14 or 24



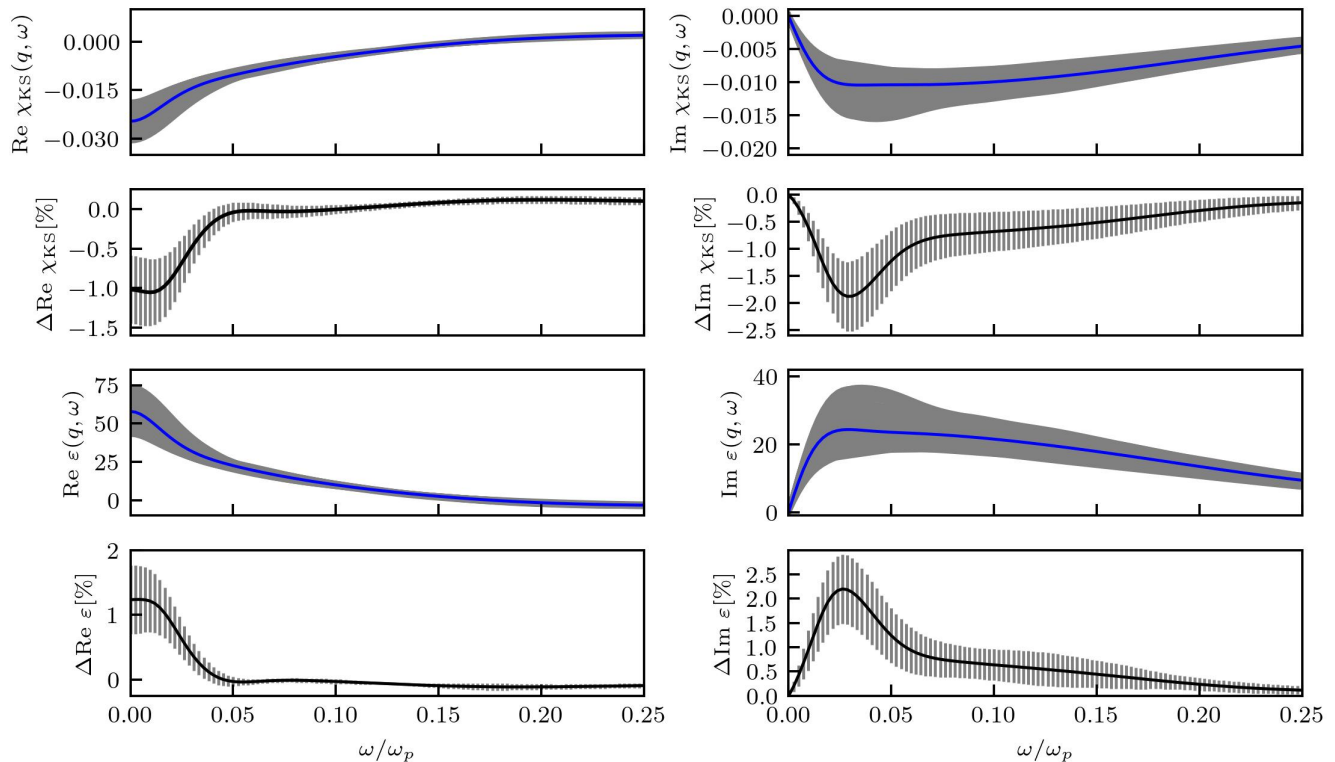


FIG. 11. First row: real and imaginary part of the macroscopic KS response function. Second row: difference between the results for the KS response function computed using different averaging methods. Third row: real and imaginary part of the dielectric function. Bottom row: difference between the results for the macroscopic dielectric function computed using different averaging methods. The results for a given snapshot are presented by grey lines (with 14 particles), and the averaged values over 250 snapshots are presented by blue lines. The results are computed for warm dense hydrogen at  $r_s = 2$  and  $\theta = 1$  for  $q/q_F \simeq 0.084$ . The standard error is depicted by vertical grey lines in the second and bottom rows.

particles. In the present work, we have demonstrated the generation of nonphysical density excitations at  $\mathbf{G} \neq 0$  in warm dense hydrogen due to finite size effects. These excitations at  $\mathbf{G} \neq 0$  can overlap with the contributions from the non-linear density responses generated at higher harmonics. Indeed, we have shown that such nonphysical density excitations at  $\mathbf{G} \neq 0$  diminish after averaging over snapshots. Therefore, the averaging is essential for the simulation of the non-linear response properties of disordered systems.

We have demonstrated that the calculation of the static XC kernel using a proper averaging procedure is important for obtaining adequate data for the XC kernel, and for the analysis of its properties. We stress that, in addition to its application in LR-TDDFT, the static XC kernel is important for a great variety of other applications such as the computation of effective interaction potentials between particles [60–63], energy loss characteristics of dense plasmas [64], and for the application within time-dependent orbital-free DFT [65] and quantum hydrodynamics [66–68].

Finally, we note that the inverse value of the macroscopic static KS response function is connected to the second order functional derivative of the non-interacting free

energy functional (kinetic energy functional at  $T = 0$ ) via the stiffness theorem [11, 66]. This relation is used to construct non-interacting free energy functionals for orbital-free DFT (OF-DFT) applications for both condensed matter [69, 70] and warm dense matter applications [71–73]. In prior works, the UEG limit at which the macroscopic KS response function reduces to the Lindhard function was used for the construction of non-interacting free energy functionals [71, 74–76]. The recipe presented in this work for the computation of the macroscopic static KS response function of real materials using the direct perturbation approach allows one to design more advanced non-interacting free energy functionals. In this way, the presented method for the macroscopic static KS response function is of relevance for other DFT applications beyond WDM.

## ACKNOWLEDGMENTS

This work was funded by the Center for Advanced Systems Understanding (CASUS) which is financed by Germany’s Federal Ministry of Education and Research (BMBF) and by the Saxon state government out of

the State budget approved by the Saxon State Parliament. This work has received funding from the European Research Council (ERC) under the European Union's Horizon 2022 research and innovation programme (Grant agreement No. 101076233, "PREX-TREME"). We gratefully acknowledge computation time at the Norddeutscher Verbund für Hoch- und Höchstleistungsrechnen (HLRN) under grant shp00026, and on the Bull Cluster at the Center for Information Services and High Performance Computing (ZIH) at Technische Universität Dresden.

## APPENDIX A

Within linear response theory for homogeneous systems, the density response function is expressed in terms of the non-interacting density response function  $\chi_0$  and the exchange-correlation kernel as [11, 13]

$$\chi(\mathbf{q}, \omega) = \frac{\chi_0(\mathbf{q}, \omega)}{1 - [v(q) + K_{xc}(\mathbf{q})] \chi_0(\mathbf{q}, \omega)}. \quad (45)$$

In the KS-DFT framework, the non-interacting density response function is given by the KS response function, i.e.,  $\chi_0 = \chi_{KS}$ . For the static case, if one substitutes Eq. (18) for the KS response function into Eq. (45) (with  $\omega = 0$ ), Eq. (10) is reproduced for the averaged value of the density response function.

In contrast, the alternative definition of the KS response function Eq. (20) is not compatible with Eq. (45). Let us for simplicity consider the case of RPA, i.e.,  $K_{xc} = 0$ . We first express the KS response function for a given snapshot in terms of the density response function by inverting Eq. (33) with  $K_{xc} = 0$ :

$$\chi_{KS, G=0}^i(\mathbf{q}) = \frac{\chi_{G=0}^i(\mathbf{q})}{1 + v(q)\chi_{G=0}^i(\mathbf{q})}, \quad (46)$$

where  $\chi_{KS, G=0}^i(\mathbf{q}) = \chi_{KS, G=0}^i(\mathbf{q}, \omega = 0)$  and  $\chi_{G=0}^i(\mathbf{q}) = \chi_{G=0}^i(\mathbf{q}, \omega = 0)$ . Using Eq. (46) in Eq. (20), we get:

$$\langle \chi_{KS}(\mathbf{q}) \rangle = \frac{1}{N_s} \sum_{i=1}^{N_s} \frac{\chi_{G=0}^i(\mathbf{q})}{1 + v(q)\chi_{G=0}^i(\mathbf{q})} \quad (47)$$

Inserting Eq. (47) and Eq. (10) into Eq. (45) then leads to the inequality

$$\chi(\mathbf{q}) = \frac{1}{N_s} \sum_{i=1}^{N_s} \chi_{G=0}^i(\mathbf{q}) \neq \frac{\langle \chi_{KS}(\mathbf{q}) \rangle}{1 - v(q)\langle \chi_{KS}(\mathbf{q}) \rangle}. \quad (48)$$

## APPENDIX B

In Fig. 12, we show the density profiles for  $N_s = 10$  snapshots with  $N = 112$  particles (solid grey lines) at  $r_s = 4$  and  $\theta = 1$  in the cases of the unperturbed and

perturbed dense hydrogen gas. From Fig. 12 a), we observe that the density deviations from the mean value are effectively reduced due to averaging over snapshots. From Fig. 12b) and Fig. 12c), one can see that the averaging of the the density perturbation over 10 snapshots effectively reduces the deviations from the cosinoidal profile.

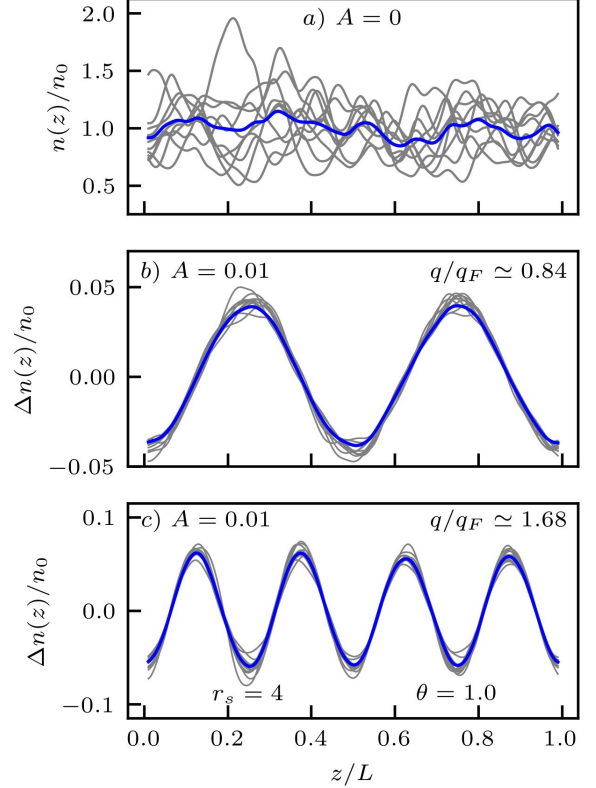


FIG. 12. a) Density distribution along the  $z$  axis of the unperturbed system, b) density perturbation at  $A = 0.01$  and  $q \simeq 0.84q_F$ , and c) density perturbation at  $A = 0.01$  and  $q \simeq 1.68q_F$ . The results are computed for  $N = 112$  particles with  $r_s = 4$  and  $\theta = 1$ .

In Fig. 13, we show the density perturbation values  $\rho_G(q)$  (as defined in Eq. (4)) at different  $G$  and  $q$  values for 112 particles. We see that the contribution of  $\rho_{G \neq 0}(q)$  components cancel each other after averaging over snapshots.

## APPENDIX C

In Fig. 14 the results for the dynamic KS response functions  $\chi_{KS}(q, \omega)$  and  $\chi_{KS, G=0}^i(q, \omega)$ , and dynamic dielectric functions  $\varepsilon_{KS}(q, \omega)$  and  $\varepsilon_{KS, G=0}^i(q, \omega)$  for  $q/q_F \simeq 0.758$  are shown. The second and bottom rows show the difference in the results computed using different averaging formulas as it is discussed in Sec. IV B. We see that the difference between different considered averaging for-

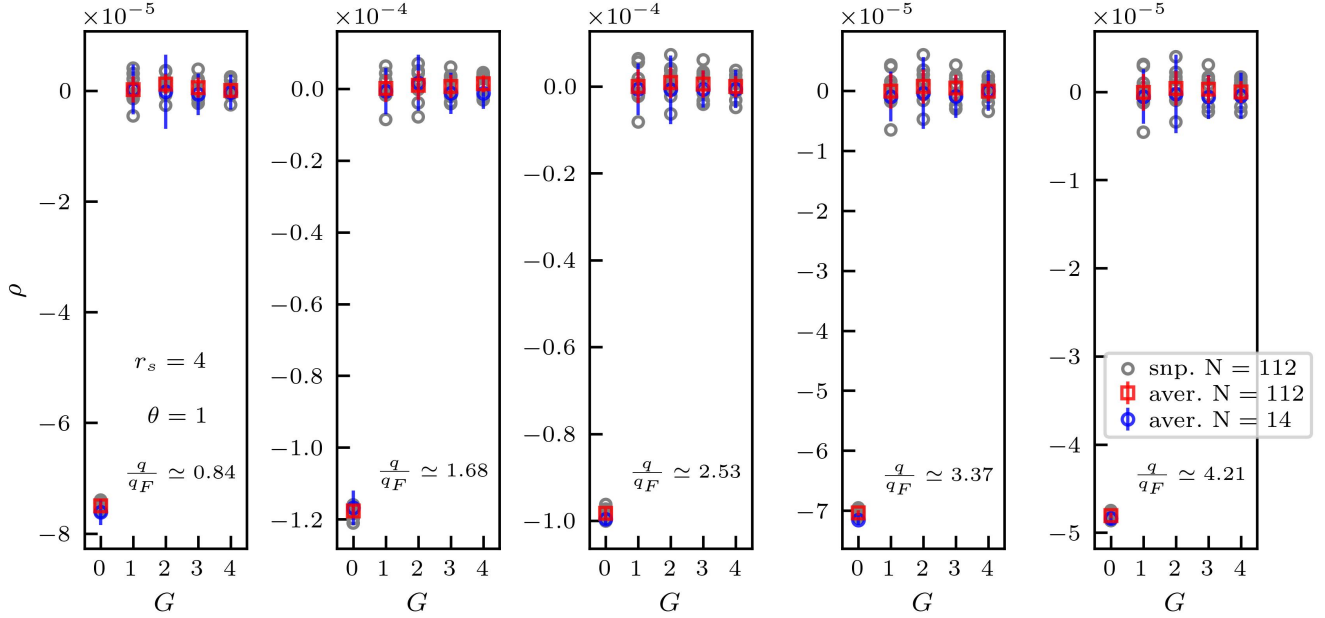


FIG. 13. Contributions to the total density change from the density perturbation values at different wavenumbers for different snapshots (the grey circles are for 112 particles), and for the averaged values over 10 snapshots with 112 particles (red) in warm dense hydrogen at  $r_s = 4$  and  $\theta = 1$ . Additionally, we show the averaged values over 10 snapshots with 14 particles (blue). The wave number  $q$  corresponds to the wavenumber of the external perturbation. The  $\mathbf{G}$  is along the  $z$ -axis and in units of  $2\pi/L$ .

mulas are negligible for  $q/q_F \simeq 0.758$ .

- 
- [1] D. Saumon, W. B. Hubbard, G. Chabrier, and H. M. van Horn, “The role of the molecular-metallic transition of hydrogen in the evolution of jupiter, saturn, and brown dwarfs,” *Astrophys. J* **391**, 827–831 (1992).
- [2] A. Becker, W. Lorenzen, J. J. Fortney, N. Nettelmann, M. Schöttler, and R. Redmer, “Ab initio equations of state for hydrogen (h-reos.3) and helium (he-reos.3) and their implications for the interior of brown dwarfs,” *Astrophys. J. Suppl. Ser* **215**, 21 (2014).
- [3] G. Chabrier, P. Brassard, G. Fontaine, and D. Saumon, “Cooling sequences and color-magnitude diagrams for cool white dwarfs with hydrogen atmospheres,” *Astrophys. J.* **543**, 216–226 (2000).
- [4] J. Daligault and S. Gupta, “Electron-ion scattering in dense multi-component plasmas: application to the outer crust of an accreting star,” *The Astrophysical Journal* **703**, 994–1011 (2009).
- [5] A. C. Hayes, M. E. Gooden, E. Henry, Gerard Jungman, J. B. Wilhelmy, R. S. Rundberg, C. Yeaman, G. Kyrala, C. Cerjan, D. L. Danielson, Jérôme Daligault, C. Wilburn, P. Volegov, C. Wilde, S. Batha, T. Bredeweg, J. L. Kline, G. P. Grim, E. P. Hartouni, D. Shaughnessy, C. Velsko, W. S. Cassata, K. Moody, L. F. Berzak Hopkins, D. Hinkel, T. Döppner, S. Le Pape, F. Graziani, D. A. Callahan, O. A. Hurricane, and D. Schneider, “Plasma stopping-power measurements reveal transition from non-degenerate to degenerate plasmas,” *Nature Physics* **16**, 432–437 (2020).
- [6] E. I. Moses, R. N. Boyd, B. A. Remington, C. J. Keane, and R. Al-Ayat, “The national ignition facility: Ushering in a new age for high energy density science,” *Physics of Plasmas* **16**, 041006 (2009).
- [7] D. A. Chapman, D. Kraus, A. L. Kritcher, B. Bachmann, G. W. Collins, R. W. Falcone, J. A. Gaffney, D. O. Gericke, S. H. Glenzer, T. M. Guylmer, J. A. Hawreliak, O. L. Landen, S. Le Pape, T. Ma, P. Neumayer, J. Nilsen, A. Pak, R. Redmer, D. C. Swift, J. Vorberger, and T. Döppner, “Simulating x-ray thomson scattering signals from high-density, millimetre-scale plasmas at the national ignition facility,” *Physics of Plasmas* **21**, 082709 (2014).
- [8] Ulf Zastra, Karen Appel, Carsten Baetz, Oliver Baehr, Lewis Batchelor, Andreas Berghäuser, Mohammadreza Banjafar, Erik Brambrink, Valerio Cerantola, Thomas E Cowan, Horst Damker, Steffen Dietrich, Samuele Di Dio Cafiso, Jörn Dreyer, Hans-Olaf Engel, Thomas Feldmann, Stefan Findeisen, Manon Foese, Daniel Fulla-Marsa, Sebastian Göde, Mohammed Hassan, Jens Hauser, Thomas Herrmannsdörfer, Hauke Höppner, Johannes Kaa, Peter Kaefer, Klaus Knöfel, Zuzana Konôpková, Alejandro Laso García, Hanns-Peter Liermann, Jona Mainberger, Mikako Makita, Eike-Christian Martens, Emma E. McBride, Dominik Möller, Motoaki Nakatsutsumi, Alexander Pelka, Christian Plueckthun, Clemens Prescher, Thomas R Preston, Michael Röper, Andreas Schmidt, Wolfgang Seidel,

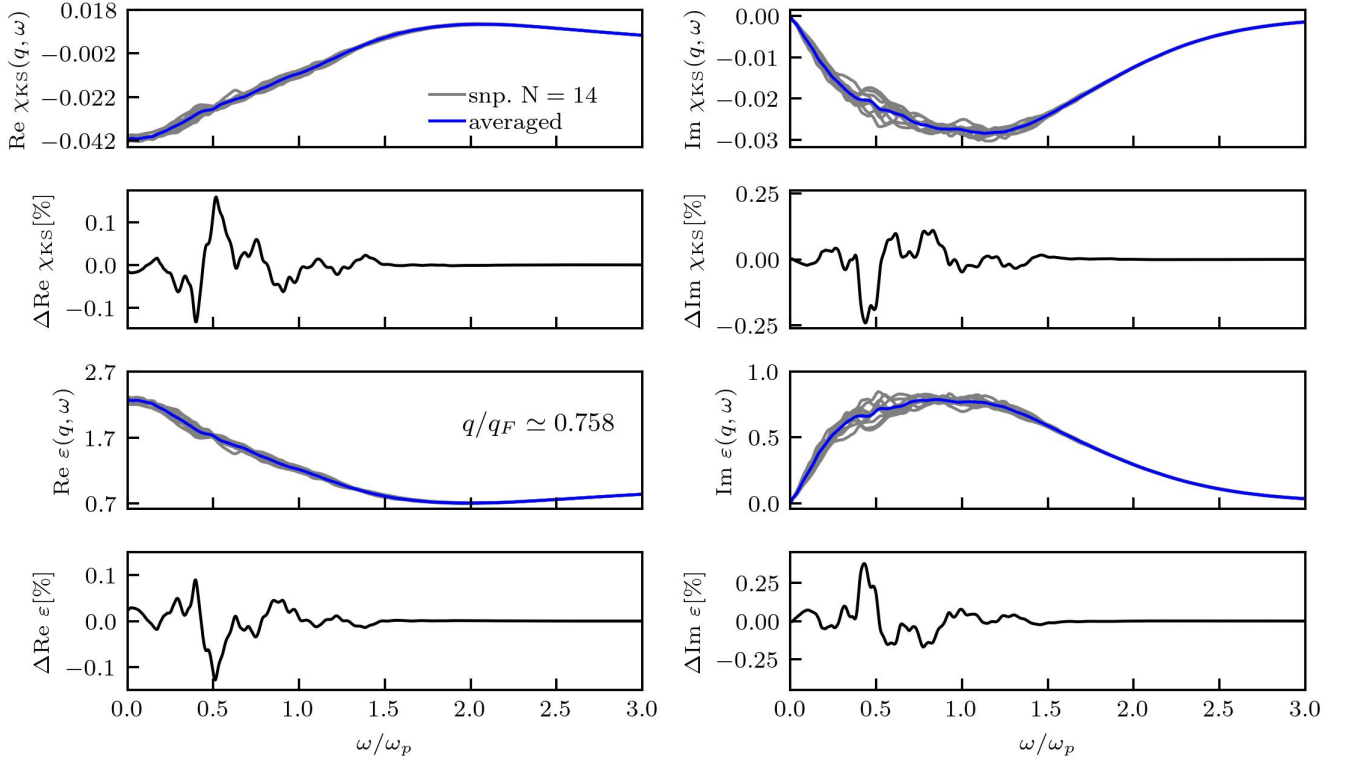


FIG. 14. First row: real and imaginary part of the macroscopic KS response function. Second row: difference between the results for the KS response function computed using different averaging methods. Third row: real and imaginary part of the dielectric function. Bottom row: difference between the results for the macroscopic dielectric function computed using different averaging methods. The results for a given snapshot are presented by grey lines (with 14 particles). The averaged values over 10 snapshots are presented by blue lines. The results are computed for warm dense hydrogen at  $r_s = 2$  and  $\theta = 1$  with  $q/q_F \simeq 0.758$ . We note that the difference between the results computed using different averaging methods is within standard error and negligible.

- Jan-Patrick Schwinkendorf, Markus O. Schoelmerich, Ulrich Schramm, Andreas Schropp, Cornelius Strohm, Konstantin Sukharnikov, Peter Talkovski, Ian Thorpe, Monika Toncian, Toma Toncian, Lennart Wollenweber, Shingo Yamamoto, and Thomas Tschentscher, “The High Energy Density Scientific Instrument at the European XFEL,” *Journal of Synchrotron Radiation* **28**, 1393–1416 (2021).
- [9] U. Zastra, P. Sperling, M. Harmand, A. Becker, T. Bornath, R. Bredow, S. Dziarzhytski, T. Fennel, L. B. Fletcher, E. F”orster, S. G”ode, G. Gregori, V. Hilbert, D. Hochhaus, B. Holst, T. Laarmann, H. J. Lee, T. Ma, J. P. Mithen, R. Mitzner, C. D. Murphy, M. Nakatsutsumi, P. Neumayer, A. Przystawik, S. Roling, M. Schulz, B. Siemer, S. Skruszewicz, J. Tiggesb”aumker, S. Toleikis, T. Tschentscher, T. White, M. W”ostmann, H. Zacharias, T. D”oppner, S. H. Glenzer, and R. Redmer, “Resolving ultrafast heating of dense cryogenic hydrogen,” *Phys. Rev. Lett* **112**, 105002 (2014).
- [10] Siegfried H. Glenzer and Ronald Redmer, “X-ray thomson scattering in high energy density plasmas,” *Rev. Mod. Phys.* **81**, 1625–1663 (2009).
- [11] G. Giuliani and G. Vignale, *Quantum Theory of the Electron Liquid* (Cambridge University Press, Cambridge, 2008).
- [12] Tobias Dornheim, Zhandos A. Moldabekov, Kushal Ramakrishna, Panagiotis Tolias, Andrew D. Baczewski, Dominik Kraus, Thomas R. Preston, David A. Chapman, Maximilian P. B”ohme, Tilo D”oppner, Frank Graziani, Michael Bonitz, Attila Cangi, and Jan Vorberger, “Electronic density response of warm dense matter,” *Physics of Plasmas* **30** (2023), 10.1063/5.0138955, 032705.
- [13] Carsten A. Ullrich, *Time-Dependent Density-Functional Theory: Concepts and Applications* (Oxford University Press, 2011).
- [14] Tobias Dornheim, Zhandos Moldabekov, Panagiotis Tolias, Maximilian B”ohme, and Jan Vorberger, “Physical insights from imaginary-time density–density correlation functions,” (2022), 10.48550/ARXIV.2209.02254.
- [15] Tobias Dornheim, Damar C. Wicaksono, Juan E. Suarez-Cardona, Panagiotis Tolias, Maximilian P. B”ohme, Zhandos A. Moldabekov, Michael Hecht, and Jan Vorberger, “Extraction of the frequency moments of spectral densities from imaginary-time correlation function data,” *Phys. Rev. B* **107**, 155148 (2023).
- [16] Tobias Dornheim, Maximilian B”ohme, Dominik Kraus, Tilo D”oppner, Thomas R. Preston, Zhandos A. Moldabekov, and Jan Vorberger, “Accurate temperature diagnostics for matter under extreme conditions,” *Nature Communications* **13**, 7911 (2022).

- [17] Tobias Dornheim, Jan Vorberger, Zhandos Moldabekov, and Maximilian Böhme, “Analyzing x-ray thomson scattering experiments of warm dense matter in the imaginary-time domain: theoretical models and simulations,” (2022), [10.48550/ARXIV.2211.00579](https://arxiv.org/abs/2211.00579).
- [18] Jan Vorberger, Thomas R. Preston, Nikita Medvedev, Maximilian P. Böhme, Zhandos A. Moldabekov, Dominik Kraus, and Tobias Dornheim, “Revealing non-equilibrium and relaxation in warm dense matter,” (2023), [10.48550/ARXIV.2302.11309](https://arxiv.org/abs/2302.11309).
- [19] Ethan W. Brown, Bryan K. Clark, Jonathan L. DuBois, and David M. Ceperley, “Path-integral monte carlo simulation of the warm dense homogeneous electron gas,” *Phys. Rev. Lett.* **110**, 146405 (2013).
- [20] Markus Holzmann, Raymond C. Clay, Miguel A. Morales, Norm M. Tubman, David M. Ceperley, and Carlo Pierleoni, “Theory of finite size effects for electronic quantum monte carlo calculations of liquids and solids,” *Phys. Rev. B* **94**, 035126 (2016).
- [21] T. Dornheim, S. Groth, T. Sjostrom, F. D. Malone, W. M. C. Foulkes, and M. Bonitz, “Ab initio quantum Monte Carlo simulation of the warm dense electron gas in the thermodynamic limit,” *Phys. Rev. Lett.* **117**, 156403 (2016).
- [22] T. Dornheim, S. Groth, and M. Bonitz, “The uniform electron gas at warm dense matter conditions,” *Phys. Reports* **744**, 1–86 (2018).
- [23] Tobias Dornheim and Jan Vorberger, “Overcoming finite-size effects in electronic structure simulations at extreme conditions,” *The Journal of Chemical Physics* **154**, 144103 (2021).
- [24] Tobias Dornheim and Jan Vorberger, “Finite-size effects in the reconstruction of dynamic properties from ab initio path integral monte carlo simulations,” *Phys. Rev. E* **102**, 063301 (2020).
- [25] Zhandos A. Moldabekov, Tobias Dornheim, and Attila Cangi, “Thermal excitation signals in the inhomogeneous warm dense electron gas,” *Scientific Reports* **12**, 1093 (2022).
- [26] Chabrier, G., “An equation of state for fully ionized hydrogen,” *J. Phys. France* **51**, 1607–1632 (1990).
- [27] Zh.A. Moldabekov, S. Groth, T. Dornheim, H. Kählert, M. Bonitz, and T. S. Ramazanov, “Structural characteristics of strongly coupled ions in a dense quantum plasma,” *Phys. Rev. E* **98**, 023207 (2018).
- [28] M.A.L. Marques, N.T. Maitra, F.M.S. Nogueira, E.K.U. Gross, and A. Rubio, *Fundamentals of Time-Dependent Density Functional Theory*, Lecture Notes in Physics (Springer Berlin Heidelberg, 2012).
- [29] Zhandos Moldabekov, Maximilian Böhme, Jan Vorberger, David Blaschke, and Tobias Dornheim, “Ab initio static exchange–correlation kernel across jacob’s ladder without functional derivatives,” *Journal of Chemical Theory and Computation* **19**, 1286–1299 (2023).
- [30] Zhandos A. Moldabekov, Michele Pavanello, Maximilian P. Böhme, Jan Vorberger, and Tobias Dornheim, “Linear-response time-dependent density functional theory approach to warm dense matter with adiabatic exchange–correlation kernels,” *Phys. Rev. Res.* **5**, 023089 (2023).
- [31] John P. Perdew and Karla Schmidt, “Jacob’s ladder of density functional approximations for the exchange–correlation energy,” *AIP Conference Proceedings* **577**, 1–20 (2001).
- [32] Zhandos A. Moldabekov, Mani Lokamani, Jan Vorberger, Attila Cangi, and Tobias Dornheim, “Non-empirical mixing coefficient for hybrid xc functionals from analysis of the xc kernel,” *The Journal of Physical Chemistry Letters* **14**, 1326–1333 (2023).
- [33] Zhandos A. Moldabekov, Mani Lokamani, Jan Vorberger, Attila Cangi, and Tobias Dornheim, “Assessing the accuracy of hybrid exchange–correlation functionals for the density response of warm dense electrons,” *The Journal of Chemical Physics* **158**, 094105 (2023).
- [34] Zhandos Moldabekov, Tobias Dornheim, Maximilian Böhme, Jan Vorberger, and Attila Cangi, “The relevance of electronic perturbations in the warm dense electron gas,” *The Journal of Chemical Physics* **155**, 124116 (2021).
- [35] Zhandos Moldabekov, Tobias Dornheim, Jan Vorberger, and Attila Cangi, “Benchmarking exchange–correlation functionals in the spin-polarized inhomogeneous electron gas under warm dense conditions,” *Phys. Rev. B* **105**, 035134 (2022).
- [36] Maximilian Böhme, Zhandos A. Moldabekov, Jan Vorberger, and Tobias Dornheim, “Static electronic density response of warm dense hydrogen: Ab initio path integral monte carlo simulations,” *Phys. Rev. Lett.* **129**, 066402 (2022).
- [37] Maximilian Böhme, Zhandos A. Moldabekov, Jan Vorberger, and Tobias Dornheim, “Ab initio path integral monte carlo simulations of hydrogen snapshots at warm dense matter conditions,” *Phys. Rev. E* **107**, 015206 (2023).
- [38] Tobias Dornheim, Maximilian Böhme, Zhandos A. Moldabekov, Jan Vorberger, and Michael Bonitz, “Density response of the warm dense electron gas beyond linear response theory: Excitation of harmonics,” *Phys. Rev. Research* **3**, 033231 (2021).
- [39] Zhandos Moldabekov, Jan Vorberger, and Tobias Dornheim, “Density functional theory perspective on the non-linear response of correlated electrons across temperature regimes,” *Journal of Chemical Theory and Computation* **18**, 2900–2912 (2022).
- [40] Tobias Dornheim, Jan Vorberger, and Michael Bonitz, “Nonlinear electronic density response in warm dense matter,” *Phys. Rev. Lett.* **125**, 085001 (2020).
- [41] T. Dornheim, S. Groth, J. Vorberger, and M. Bonitz, “Permutation blocking path integral Monte Carlo approach to the static density response of the warm dense electron gas,” *Phys. Rev. E* **96**, 023203 (2017).
- [42] Christian Kollmar and Frank Neese, “The static response function in kohn-sham theory: An appropriate basis for its matrix representation in case of finite ao basis sets,” *The Journal of Chemical Physics* **141**, 134106 (2014).
- [43] S. Groth, T. Dornheim, T. Sjostrom, F. D. Malone, W. M. C. Foulkes, and M. Bonitz, “Ab initio exchange–correlation free energy of the uniform electron gas at warm dense matter conditions,” *Phys. Rev. Lett.* **119**, 135001 (2017).
- [44] A. D. Baczewski, L. Shulenburger, M. P. Desjarlais, S. B. Hansen, and R. J. Magyar, “X-ray thomson scattering in warm dense matter without the chihara decomposition,” *Phys. Rev. Lett.* **116**, 115004 (2016).
- [45] Xavier Gonze, Bernard Amadon, Gabriel Antonius, Frédéric Arnardi, Lucas Baguet, Jean-Michel Beuken, Jordan Bieder, François Bottin, Johann Bouchet, Eric Bousquet, Nils Brouwer, Fabien Bruneval, Guillaume



- Brunin, Théo Cavignac, Jean-Baptiste Charraud, Wei Chen, Michel Côté, Stefaan Cottener, Jules Denier, Grégory Geneste, Philippe Ghosez, Matteo Giantomassi, Yannick Gillet, Olivier Gingras, Donald R. Hamann, Geoffroy Hautier, Xu He, Nicole Helbig, Natalie Holzwarth, Yongchao Jia, François Jollet, William Lafargue-Dit-Hauret, Kurt Lejaeghere, Miguel A. L. Marques, Alexandre Martin, Cyril Martins, Henrique P. C. Miranda, Francesco Naccarato, Kristin Persson, Guido Petretto, Valentin Planes, Yann Pouillon, Sergei Prokhorenko, Fabio Ricci, Gian-Marco Rignanese, Aldo H. Romero, Michael Marcus Schmitt, Marc Torrent, Michiel J. van Setten, Benoit Van Troeye, Matthieu J. Verstraete, Gilles Zerah, and Josef W. Zwanziger, “The abinit project: Impact, environment and recent developments,” *Comput. Phys. Commun.* **248**, 107042 (2020).
- [46] Aldo H. Romero, Douglas C. Allan, Bernard Amadon, Gabriel Antonius, Thomas Applencourt, Lucas Baguet, Jordan Bieder, François Bottin, Johann Bouchet, Eric Bousquet, Fabien Bruneval, Guillaume Brunin, Damien Caliste, Michel Côté, Jules Denier, Cyrus Dreyer, Philippe Ghosez, Matteo Giantomassi, Yannick Gillet, Olivier Gingras, Donald R. Hamann, Geoffroy Hautier, François Jollet, Gérard Jomard, Alexandre Martin, Henrique P. C. Miranda, Francesco Naccarato, Guido Petretto, Nicholas A. Pike, Valentin Planes, Sergei Prokhorenko, Tonatiuh Rangel, Fabio Ricci, Gian-Marco Rignanese, Miquel Royo, Massimiliano Stengel, Marc Torrent, Michiel J. van Setten, Benoit Van Troeye, Matthieu J. Verstraete, Julia Wiktor, Josef W. Zwanziger, and Xavier Gonze, “Abinit: Overview, and focus on selected capabilities,” *J. Chem. Phys.* **152**, 124102 (2020).
- [47] X. Gonze, F. Jollet, F. Abreu Araujo, D. Adams, B. Amadon, T. Applencourt, C. Audouze, J.-M. Beuken, J. Bieder, A. Bokhanchuk, E. Bousquet, F. Bruneval, D. Caliste, M. Côté, F. Dahm, F. Da Pieve, M. Delaveau, M. Di Gennaro, B. Dorado, C. Espejo, G. Geneste, L. Genovese, A. Gerossier, M. Giantomassi, Y. Gillet, D.R. Hamann, L. He, G. Jomard, J. Laflamme Janssen, S. Le Roux, A. Levitt, A. Lherbier, F. Liu, I. Lukačević, A. Martin, C. Martins, M.J.T. Oliveira, S. Poncé, Y. Pouillon, T. Rangel, G.-M. Rignanese, A.H. Romero, B. Rousseau, O. Rubel, A.A. Shukri, M. Stankovski, M. Torrent, M.J. Van Setten, B. Van Troeye, M.J. Verstraete, D. Waroquiers, J. Wiktor, B. Xu, A. Zhou, and J.W. Zwanziger, “Recent developments in the ABINIT software package,” *Comput. Phys. Commun.* **205**, 106–131 (2016).
- [48] X. Gonze, B. Amadon, P.-M. Anglade, J.-M. Beuken, F. Bottin, P. Boulanger, F. Bruneval, D. Caliste, R. Caracas, M. Côté, T. Deutsch, L. Genovese, Ph. Ghosez, M. Giantomassi, S. Goedecker, D.R. Hamann, P. Hermet, F. Jollet, G. Jomard, S. Leroux, M. Mancini, S. Mazevet, M.J.T. Oliveira, G. Onida, Y. Pouillon, T. Rangel, G.-M. Rignanese, D. Sangalli, R. Shaltaf, M. Torrent, M.J. Verstraete, G. Zerah, and J.W. Zwanziger, “ABINIT: First-principles approach to material and nanosystem properties,” *Comput. Phys. Commun.* **180**, 2582–2615 (2009).
- [49] X. Gonze, G.-M. Rignanese, M. Verstraete, J.-M. Beuken, Y. Pouillon, R. Caracas, F. Jollet, M. Torrent, G. Zerah, M. Mikami, Ph. Ghosez, M. Veithen, J.-Y. Raty, V. Olevano, F. Bruneval, L. Reining, R. Godby, G. Onida, and D.R. Hamann D.C. Allan, “A brief introduction to the ABINIT software package,” *Zeitschrift für Kristallographie - Crystalline Materials* **220**, 558–562 (2005).
- [50] X. Gonze, J.-M. Beuken, R. Caracas, F. Detraux, M. Fuchs, G.-M. Rignanese, L. Sindic, M. Verstraete, G. Zerah, F. Jollet, M. Torrent, A. Roy, M. Mikami, Ph. Ghosez, J.-Y. Raty, and D.C. Allan, “First-principles computation of material properties: The ABINIT software project,” *Computational Materials Science* **25**, 478–492 (2002).
- [51] John P. Perdew, Kieron Burke, and Matthias Ernzerhof, “Generalized gradient approximation made simple,” *Physical Review Letters* **77**, 3865–3868 (1996).
- [52] Lenz Fiedler, Zhandos A. Moldabekov, Xuecheng Shao, Kaili Jiang, Tobias Dornheim, Michele Pavanello, and Attila Cangi, “Accelerating equilibration in first-principles molecular dynamics with orbital-free density functional theory,” *Phys. Rev. Research* **4**, 043033 (2022).
- [53] Jun Yan, Jens. J. Mortensen, Karsten W. Jacobsen, and Kristian S. Thygesen, “Linear density response function in the projector augmented wave method: Applications to solids, surfaces, and interfaces,” *Phys. Rev. B* **83**, 245122 (2011).
- [54] Zhandos Moldabekov, Tobias Dornheim, Maximilian Böhme, Jan Vorberger, and Attila Cangi, “The relevance of electronic perturbations in the warm dense electron gas,” *The Journal of Chemical Physics* **155**, 124116 (2021).
- [55] B. Militzer and D. M. Ceperley, “Path integral monte carlo simulation of the low-density hydrogen plasma,” *Phys. Rev. E* **63**, 066404 (2001).
- [56] A. A. Kugler, “Theory of the local field correction in an electron gas,” *J. Stat. Phys.* **12**, 35 (1975).
- [57] A. Seidl, A. Görling, P. Vogl, J. A. Majewski, and M. Levy, “Generalized kohn-sham schemes and the band-gap problem,” *Phys. Rev. B* **53**, 3764–3774 (1996).
- [58] Stephan Kümmel and Leor Kronik, “Orbital-dependent density functionals: Theory and applications,” *Rev. Mod. Phys.* **80**, 3–60 (2008).
- [59] Rachel Garrick, Amir Natan, Tim Gould, and Leor Kronik, “Exact generalized kohn-sham theory for hybrid functionals,” *Phys. Rev. X* **10**, 021040 (2020).
- [60] Tobias Dornheim, Panagiotis Tolias, Zhandos A. Moldabekov, Attila Cangi, and Jan Vorberger, “Effective electronic forces and potentials from ab initio path integral monte carlo simulations,” *The Journal of Chemical Physics* **156**, 244113 (2022).
- [61] Zhandos A. Moldabekov, Tobias Dornheim, and Michael Bonitz, “Screening of a test charge in a free-electron gas at warm dense matter and dense non-ideal plasma conditions,” *Contributions to Plasma Physics*, e202000176 (2021).
- [62] Zh.A. Moldabekov, S. Groth, T. Dornheim, M. Bonitz, and T.S. Ramazanov, “Ion potential in non-ideal dense quantum plasmas,” *Contributions to Plasma Physics* **57**, 532–538 (2017).
- [63] Zh.A. Moldabekov, H. Kählert, T. Dornheim, S. Groth, M. Bonitz, and T. S. Ramazanov, “Dynamical structure factor of strongly coupled ions in a dense quantum plasma,” *Phys. Rev. E* **99**, 053203 (2019).
- [64] Zh. A. Moldabekov, T. Dornheim, M. Bonitz, and T. S. Ramazanov, “Ion energy-loss characteristics and friction in a free-electron gas at warm dense matter and non-ideal dense plasma conditions,” *Phys. Rev. E* **101**, 053203 (2020).

- (2020).
- [65] Fabio Della Sala, “Orbital-free methods for plasmonics: Linear response,” *The Journal of Chemical Physics* **157**, 104101 (2022).
- [66] Zh. A. Moldabekov, M. Bonitz, and T. S. Ramazanov, “Theoretical foundations of quantum hydrodynamics for plasmas,” *Physics of Plasmas* **25**, 031903 (2018).
- [67] Z. A. Moldabekov, T. Dornheim, G. Gregori, F. Graziani, M. Bonitz, and A. Cangi, “Towards a quantum fluid theory of correlated many-fermion systems from first principles,” *SciPost Phys.* **12**, 062 (2022).
- [68] F. Graziani, Z. Moldabekov, B. Olson, and M. Bonitz, “Shock physics in warm dense matter: A quantum hydrodynamics perspective,” *Contributions to Plasma Physics* **62**, e202100170 (2022).
- [69] Yan Alexander Wang and Emily A Carter, “Orbital-free kinetic-energy density functional theory,” *Theoretical methods in condensed phase chemistry*, 117–184 (2002).
- [70] Zhandos A. Moldabekov, Xuecheng Shao, Michele Pavanello, Jan Vorberger, Frank Graziani, and Tobias Dornheim, “Imposing correct jellium response is key to predict linear and non-linear density response by orbital-free dft,” (2023), [arXiv:2304.11169](https://arxiv.org/abs/2304.11169) [physics.comp-ph].
- [71] Travis Sjoström and Jérôme Daligault, “Nonlocal orbital-free noninteracting free-energy functional for warm dense matter,” *Phys. Rev. B* **88**, 195103 (2013).
- [72] Alexander J. White, Ondrej Certik, Y. H. Ding, S. X. Hu, and Lee A. Collins, “Time-dependent orbital-free density functional theory for electronic stopping power: Comparison to the mermin-kohn-sham theory at high temperatures,” *Phys. Rev. B* **98**, 144302 (2018).
- [73] Y. H. Ding, A. J. White, S. X. Hu, O. Certik, and L. A. Collins, “Ab initio studies on the stopping power of warm dense matter with time-dependent orbital-free density functional theory,” *Phys. Rev. Lett.* **121**, 145001 (2018).
- [74] Wenhui Mi, Alessandro Genova, and Michele Pavanello, “Nonlocal kinetic energy functionals by functional integration,” *The Journal of Chemical Physics* **148**, 184107 (2018).
- [75] Wenhui Mi and Michele Pavanello, “Orbital-free density functional theory correctly models quantum dots when asymptotics, nonlocality, and nonhomogeneity are accounted for,” *Physical Review B* **100**, 041105 (2019).
- [76] Lucian A. Constantin, Eduardo Fabiano, and Fabio Della Sala, “Semilocal pauli–gaussian kinetic functionals for orbital-free density functional theory calculations of solids,” *The Journal of Physical Chemistry Letters* **9**, 4385–4390 (2018).